

EVOLUTION AND ENVIRONMENT OF EARLY-TYPE GALAXIES

MARIANGELA BERNARDI,¹ ROBERT C. NICHOL,² RAVI K. SHETH,¹ C. J. MILLER,³ AND J. BRINKMANN⁴

Received 2004 September 13; accepted 2005 September 8

ABSTRACT

Chemical abundance indicators are studied using composite spectra, which we provide in tabular form. Tables of line strengths measured from these spectra and parameters derived from these line strengths are also provided. From these we find that at fixed luminosity, early-type galaxies in low-density environments are slightly bluer, with stronger O II emission and stronger H δ and H γ Balmer absorption lines, indicative of star formation in the not very distant past. These galaxies also tend to have systematically weaker D4000 indices. The Lick indices and α -element abundance indicators correlate weakly but significantly with environment. For example, at fixed velocity dispersion, Mg is weaker in early-type galaxies in low-density environments by 30% of the rms scatter across the full sample, whereas most Fe indicators show no significant environmental dependence. The galaxies in our sample span a redshift range that corresponds to look-back times of ~ 1 Gyr. We see clear evidence for evolution of line-index strengths over this time. Since the low-redshift population is almost certainly a passively aged version of the more distant population, age is likely the main driver for any observed evolution. We use the observed redshift evolution as a model-independent clock to identify indicators that are more sensitive to age than to other effects such as metallicity. In principle, for a passively evolving population, comparison of the trends with redshift and environment constrain how strongly the luminosity-weighted ages and metallicities depend on environment. We develop a method for doing this that does not depend on the details of stellar population synthesis models. Our analysis suggests that the galaxies that populate the densest regions in our sample are older by ~ 1 Gyr than objects of the same luminosity in the least dense regions, and that metallicity differences are negligible. We also use single-burst stellar population synthesis models, which allow for nonsolar α -element abundance ratios, to interpret our data. The combination of H β , Mg b , and $\langle \text{Fe} \rangle$ lines suggests that age, metallicity, and α -enhancement all increase with velocity dispersion. The objects at lower redshifts are older but have the same metallicities and α -enhancements as their counterparts of the same σ at higher redshifts, as expected if the low-redshift sample is a passively aged version of the sample at higher redshifts. In addition, objects in dense environments are less than 1 Gyr older and α -enhanced by ~ 0.02 relative to their counterparts of the same velocity dispersion in less dense regions, but the metallicities show no dependence on environment. This suggests that in dense regions, the stars in early-type galaxies formed at slightly earlier times and on a slightly shorter timescale than in less dense regions. Using H γ_F instead of H β leads to slightly younger ages but the same qualitative differences between environments. In particular, we find no evidence that objects in low-density regions are more metal-rich.

Key words: galaxies: elliptical and lenticular, cD — galaxies: evolution — galaxies: fundamental parameters — galaxies: photometry — galaxies: stellar content

Online material: color figures, machine-readable tables, tar file

1. INTRODUCTION

There are two competing scenarios for the formation and evolution of giant early-type galaxies: either they formed from an early monolithic collapse, and have evolved passively since, or they formed from the stochastic mergers of smaller systems. Both scenarios predict that the observed properties of galaxies should correlate with their environments.

In the first scenario, correlations with environment may arise because of a host of plausible physical effects associated with dense environments: these include ram pressure stripping of gas due to the hot, intracluster medium (Gunn & Gott 1972), galaxy harassment (Moore et al. 1999), tidal interactions (Bekki et al.

2001) and strangulation (Balogh et al. 2001). In the second scenario such effects may also be important, but there is another natural reason to expect correlations with environment. In hierarchical clustering models, the oldest stars in the present day universe likely formed in the most massive systems present at high redshift (White & Rees 1978; White & Frenk 1991), and those massive high-redshift systems merged with one another to form the most massive systems at the present time (Lacey & Cole 1993), so that, at any given time, the most massive systems populate the densest regions (Mo & White 1996). Hence, the oldest stars, and the most massive galaxies, should populate the densest regions; since mass and age influence early-type galaxy observables, a correlation with environment is expected (Kauffmann 1996; Kauffmann & Charlot 1998). Since the two scenarios may make different predictions for trends with environment, it is interesting to quantify such trends. Our goal in what follows is not so much to distinguish between these models as to develop techniques that allow one to quantify and interpret environmental trends, since both models predict that trends should exist.

Many early-type galaxy observables correlate with one another. Among the best studied are the color-magnitude relation

¹ Department of Physics and Astronomy, University of Pennsylvania, Philadelphia, PA 19104.

² Institute of Cosmology and Gravitation, Mercantile House, Hampshire Terrace, University of Portsmouth, Portsmouth PO1 2EG, UK.

³ Cerro Tololo Inter-American Observatory, NOAO, Casilla 603, La Serena, Chile.

⁴ Apache Point Observatory, 2001 Apache Point Road, P.O. Box 59, Sunspot, NM 88349-0059.

(e.g., Sandage & Visvanathan 1978a, 1978b; Bower et al. 1992a, 1992b), the luminosity-velocity dispersion relation (Poveda 1961; Faber & Jackson 1976), the Fundamental Plane (Dressler et al. 1987; Djorgovski & Davis 1987), and correlations between chemical abundance indicators such as Mg and the velocity dispersion (e.g., Jørgensen 1997; Bernardi et al. 1998; Colless et al. 1999; Kuntschner et al. 2001). The search for correlations with environment has generally taken the form of measuring some of these correlations and then trying to quantify whether the relation in dense cluster-like regions is different from in less dense regions. For instance, the Mg- σ relation shows only a weak dependence on environment (Bernardi et al. 1998), and recent work with the Sloan Digital Sky Survey (SDSS) indicates that the color-magnitude relation also shows little dependence on environment (Bernardi et al. 2003d; Hogg et al. 2004; Balogh et al. 2004; Wake et al. 2005).

Interpreting these weak differences is more complicated. It is not clear whether the small differences reflect genuinely small differences in the ages and metallicities of galaxies in low- and high-density environments or whether large changes in age are compensated for by changes in metallicity (e.g., Worthey et al. 1994; Kuntschner et al. 2001), leaving the observables essentially unchanged. In addition, because early types evolve relatively rapidly only when they are younger than a few gigayears, small differences in formation times lead to only small differences in observables at later times.

In this study we attempt to separate out the effects of age from other effects in two ways. In the first method we study the spectroscopic and photometric properties of massive early-type galaxies over a wide range in environment and over a relatively small range in redshift. The small redshift range helps ensure that the galaxy population at the low-redshift end of the sample is essentially a passively aged version of the population at higher redshifts. Comparison of the observed evolution with the observed dependence on environment provides a relatively model-independent estimate of the typical age differences between environments. Our second method is more model dependent. We compare a variety of absorption-line strengths in the spectra of early-type galaxies with the latest generation of stellar population synthesis models. These models account for the fact that early-type galaxies are α -enhanced relative to solar (e.g., Tripicco & Bell 1995; Trager et al. 2000; Thomas et al. 2003, hereafter TMB03; Thomas et al. 2004, hereafter TMK04; Tantalo & Chiosi 2004).

The requirements of relatively small redshift coverage but relatively large numbers of galaxies with well-calibrated photometry and spectroscopy (so that small evolutionary and environmental trends can be detected) make the SDSS (York et al. 2000) the ideal database for this study. Section 2 describes various aspects of the data set: how the early-type galaxy sample was selected (similar to Bernardi et al. 2003a), how composite spectra suitable for line-index measurements were assembled (similar to Bernardi et al. 2003d), and how estimates of the local environment for each galaxy were made. Section 3 presents evidence from the Fundamental Plane that cluster galaxies are slightly different from their counterparts in low-density regions. Correlations between environment and various chemical abundance indicators are studied in § 4. Section 5 compares the dependence on environment with that on redshift and discusses how these observed trends can begin to distinguish age effects from those associated with changes in metallicity. It then provides a more quantitative argument that does not depend on the use of stellar population synthesis models. Such models are used to interpret our data in § 6. Section 7 summarizes our findings and discusses some

implications. Appendices A and B discuss how we correct for selection effects and flux calibration issues, respectively. Tables of the composite spectra we use, the line strengths measured from them, and the ages, metallicities, and α -element abundance ratios derived from the line strengths are available, in their entirety, in the electronic version of the journal. Where necessary, we assume a background cosmological model that is flat, with matter accounting for 30% of the critical density and a Hubble constant at the present time of $H_0 = 70 \text{ km s}^{-1} \text{ Mpc}^{-1}$.

2. SAMPLE SELECTION

All the objects we analyze were selected from the SDSS database. See York et al. (2000) for a technical summary of the SDSS project; Stoughton et al. (2002) for a description of the Early Data Release; Abazajian et al. (2003) et al. for a description of DR1, the First Data Release; Gunn et al. (1998) for details about the camera; Fukugita et al. (1996), Hogg et al. (2001), and Smith et al. (2002) for details of the photometric system and calibration; Lupton et al. (2001) for a discussion of the photometric data reduction pipeline; Pier et al. (2003) for the astrometric calibrations; Blanton et al. (2003) for details of the tiling algorithm; and Strauss et al. (2002) and Eisenstein et al. (2001) for details of the target selection.

We selected all objects targeted as galaxies and having Petrosian (1976) apparent magnitude $14.5 \leq r_{\text{Pet}} \leq 17.75$. To extract a sample of early-type galaxies, we then chose the subset with the spectroscopic parameter $\text{eclass} < 0$, which classifies the spectral type based on a principal component analysis, and the photometric parameter $\text{fracDev}_r > 0.8$, which is a seeing-corrected indicator of morphology. The parameter fracDev_r is obtained by taking the best-fit exponential and de Vaucouleurs fits to the surface brightness profile, finding the linear combination of the two that best fits the image, and storing the fraction contributed by the de Vaucouleurs fit. We removed galaxies with problems in the spectra (using the `zStatus` and `zWarning` flags). From this subsample we finally chose those objects for which the spectroscopic pipeline had measured velocity dispersions (meaning that the signal-to-noise ratio in pixels between the rest-frame wavelengths of 4200 and 5800 Å is $\text{S/N} > 10$). This gave a sample of 39,320 objects, with photometric parameters output by version V5.4 of the SDSS photometric pipeline and V.23 reductions of the spectroscopic pipeline. For reasons given in Bernardi et al. (2003a), the luminosities and sizes we use in what follows are *not* derived from Petrosian quantities, but from fits of de Vaucouleurs profiles to the images.

2.1. Local Environment

There is some debate in the recent literature over the optimal method for defining the local environment of galaxies (Eisenstein 2003; Kauffmann et al. 2003; Balogh et al. 2004). The options include using catalogs of clusters and groups of galaxies, adaptive measurements of local galaxy density, such as distance to the n th nearest neighbor, and physical measurements of density based on expectation from simulations. Each of these methods has its own set of pros and cons. In this study we attempt to minimize the problems associated with any one of these measurements of environment by using a combination.

We have chosen to represent the environment of a galaxy in two ways. One is to estimate the comoving distance to the nearest cluster, and the other defines a local density proportional to the inverse of the volume that encloses the nearest 10 galaxies at $M_r < -21.5$ (Petrosian magnitudes). As our sample is magnitude-limited, and the abundance of luminous galaxies

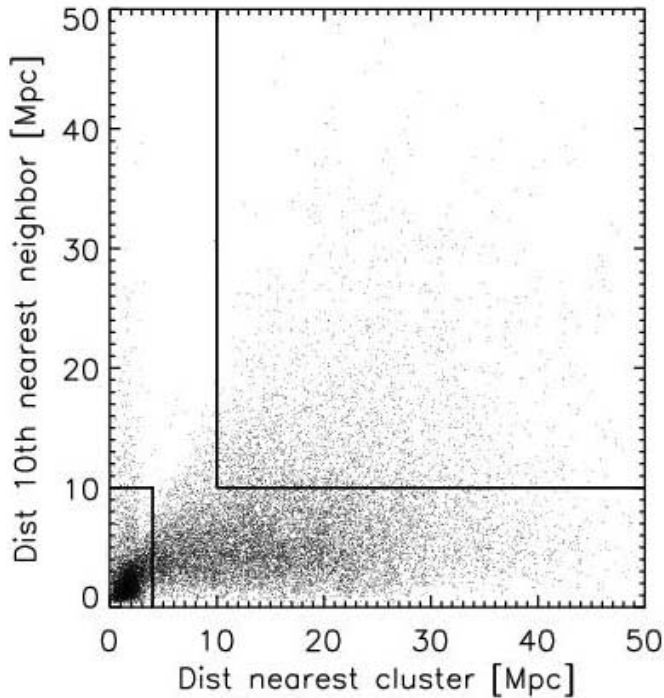


FIG. 1.—Classification into high-density (*lower left*) and low-density environments (*upper right*) based on the comoving distance to the 10th nearest luminous ($L > 3L_*$) neighbor, and on the comoving distance to the nearest massive cluster in the C4 catalog (Miller et al. 2005; each cluster is more luminous than $1.75 \times 10^{11} h^{-2} L_\odot \sim 10L_*$).

drops exponentially at the bright end, the sample is much sparser at high redshifts. As a result, distances to the n th nearest neighbor will all be larger at high redshifts, unless we also specify that all n neighbors are sufficiently luminous that they would have been seen at all redshifts in our catalog. Our brightness cut was chosen to satisfy the competing constraints of having enough objects from which to estimate distances, and of ensuring that those objects would satisfy the SDSS magnitude limits over as wide a range as possible. Since such objects cannot be seen beyond $z = 0.15$, we limit our catalog to $z \leq 0.14$.

For each galaxy in our sample, we estimate comoving (three-dimensional) distances to all objects more luminous than $1.75 \times 10^{11} h_{100}^{-2} L_\odot$ in the C4 cluster catalog (Miller et al. 2005). This catalog is more than 90% complete out to $z = 0.14$. Estimates of the mean redshift z_{cl} , virial radius r_{cl} , and velocity dispersion σ_{cl} are available for each C4 cluster. Given the redshift, the virial radius defines an angular scale, θ_{cl} . We label as cluster galaxies all those that lie within θ_{cl} and $3 \sigma_{cl}$ of a C4 cluster.

The typical absolute magnitude of the early-type galaxies in our catalog is $M_r \simeq -21$. The absolute magnitude of the Sun is 4.62 in this band, so the luminosity of a typical early type is $\sim 1.77 \times 10^{10} h_{70}^{-2} L_\odot$; the C4 clusters are ~ 10 times more luminous than a typical early-type galaxy. This means that smaller groups are *not* included in the C4 catalog; early-type galaxies in such groups will be assigned to denser environments only if such groups typically cluster around C4 clusters. Since such group members inhabit environments that are intermediate between rich clusters and low-density environments, if we wish to define a sample in low-density environments we would like to include as few group galaxies as possible.

With this in mind, we define a sample of galaxies in less dense environments when the distance to the nearest cluster *and* the distance to the 10th nearest neighbor galaxy are larger than 10 Mpc. Our cut on 10th neighbor distance is supposed to eliminate most group galaxies from our low-density environment sample. Thus, only objects in the densest (*lower left*) and least dense (*upper right*) environments of Figure 1 are used in the analysis that follows: in all there were 3112 and 5711 early types in the two environments at $z \leq 0.14$.

There is a supercluster in the SDSS sample at $z \sim 0.08$. In what follows we see some peculiarities in the redshift bin that contains this structure, so it may be that our estimates of environmental effects are altered by the supercluster.

2.2. Line Indices

Later in this paper we study how various chemical abundance indicators of the early-type galaxy population depend on redshift and environment. The typical S/N of an individual SDSS spectrum in our sample, ~ 18 , is considerably smaller than the value (~ 50) required to make reliable estimates of line strengths. Therefore, for each environment we construct high-S/N composite spectra suitable for line-index measurements by co-adding the spectra of similar objects. We use narrow bins in luminosity, size, velocity dispersion, and redshift, chosen so that the resulting composite spectra had S/Ns of ~ 100 . See Bernardi et al. (2003d) for details of the co-addition procedure. Briefly, spectra are normalized to have the same flux between 3900 and 7000 Å and then co-added, weighting by the observed error estimate in each pixel. Table 1 describes the bins we have chosen. The 925 composite spectra themselves are available from the electronic edition of the journal. Figure 2 shows the distribution of the number of objects per composite, as well as the distribution of S/Ns. The results that follow have been obtained by using all the composites, although we have checked that the main conclusions do not change if only the subset with $S/N > 40$ is used. Figure 2 (*left*) shows the difference between the full set of composites and the higher S/N subset.

TABLE 1
COMPOSITE SPECTRA

ID	ID _z	$\langle z \rangle$	ID _M	$\langle M_r \rangle$ (mag)	$\langle M_i \rangle$ (mag)	ID _σ	$\langle \log \sigma \rangle$ (km s ⁻¹)	ID _R	$\langle \log R \rangle$ (kpc h ⁻¹)	$\langle g-r \rangle$ (mag)	$\langle \text{fracDev} \rangle$	Env.	N _g	S/N
1.....	1	0.0593	1	-19.873	-20.240	3	2.131	2	0.119	0.70	0.98	1	3	32
2.....	1	0.0615	2	-20.147	-20.477	3	2.120	1	0.058	0.72	0.98	1	3	37
3.....	1	0.0629	2	-20.204	-20.513	4	2.178	1	0.075	0.78	0.97	1	2	28
4.....	1	0.0634	2	-20.244	-20.629	5	2.228	1	0.047	0.79	0.97	1	5	53
5.....	1	0.0602	2	-20.349	-20.720	6	2.266	1	0.028	0.74	1.00	1	2	49

NOTES.—Mean values of redshift, evolution-corrected absolute magnitudes, velocity dispersion, effective radius, color, fracDev, and environment (0 and 1 indicate low- and high-density environments), as well as the number of galaxies and the mean S/N for the objects that make up each composite, are given. Table 1 is published in its entirety in the electronic edition of the *Astronomical Journal*. A portion is shown here for guidance regarding its form and content.

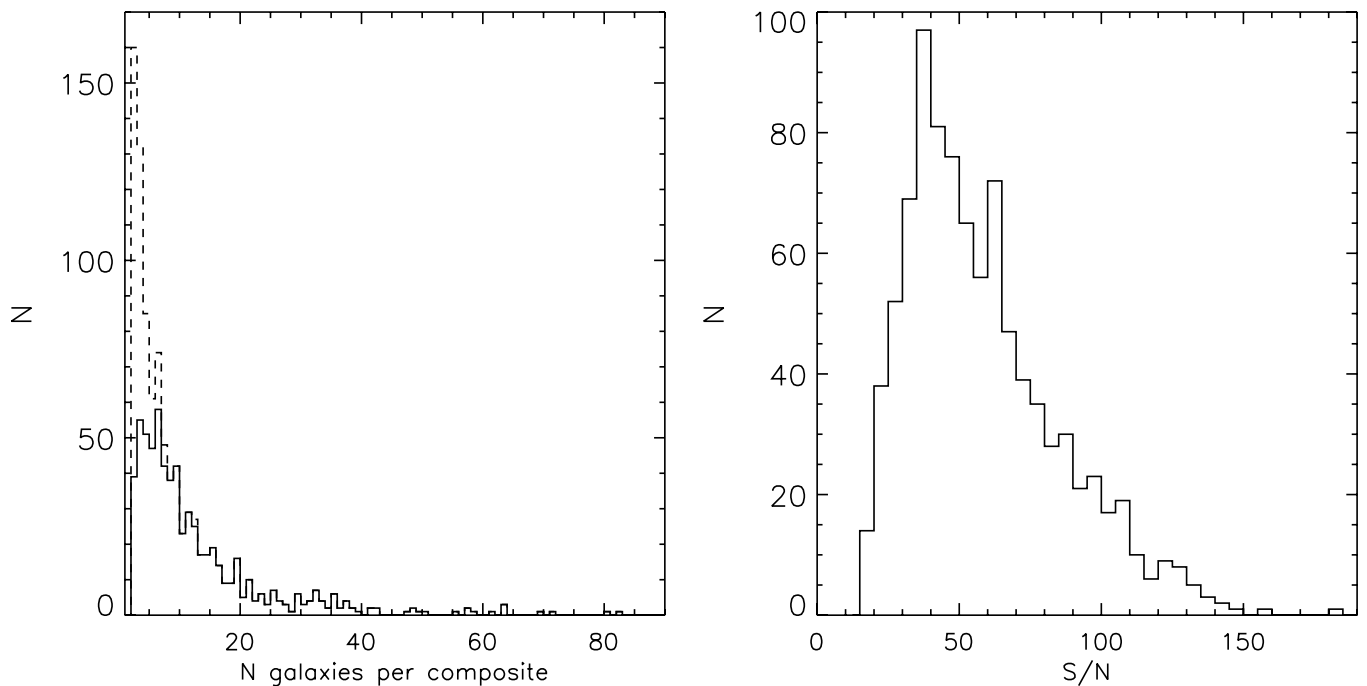


FIG. 2.—Distribution of the number of galaxies in a composite spectrum (*left*) and the S/Ns of the composites (*right*). The dashed histogram in the left panel shows all composites, and the solid histogram shows those with $S/N \geq 40$.

We measure the strengths of the original Lick indices (Worthey et al. 1994; Trager et al. 1998), as well as a number of other spectral features in each composite. This is because, with the exception of $H\beta$, none of the Lick indices are particularly sensitive to recent star formation. Although we do not expect to find objects with large star formation rates in our sample, some of the objects in it may have been forming stars at relatively small look-back times. Therefore, we also study some Balmer lines in absorption, $H\delta_A$, $H\delta_F$, $H\gamma_A$, and $H\gamma_F$, defined following Worthey & Ottaviani (1997), which are expected to indicate star formation activity in the less distant past. Our estimates of the Balmer line strengths should be treated as lower limits because they may be filled in by emission for which we have not corrected. However, we do correct $H\beta$ by adding 0.05 times the equivalent width of the $O\ II$ line to the measured value. The standard correction uses $O\ III$ (e.g., Trager et al. 1998), but this is very noisy in our sample: $O\ II$ shows a cleaner correlation.

In addition, many of these lines are close to the edge of the SDSS spectrograph, where flux calibration problems may bias our measurements. We discuss this more fully shortly.

Although our sample selection excludes strong emission lines, some weak emission is permitted. We find weak emission in $O\ II$, which indicates very recent star formation, and/or active galactic nucleus (AGN) activity. We also study the strength of the break at 4000 Å and combinations of indices that are expected to be indicators of the metallicity and the relative abundances of α -elements.

Where available (e.g., Jørgensen 1997), small aperture corrections have been applied to the measured values. These corrections are typically of the form $(8r/r_e)^\alpha$ with $|\alpha| \sim 0.05$ (where r_e is the half-light radius). Where no prescription was available in the literature, we used $|\alpha| = 0.05$. This correction only matters for the trends with redshift presented in § 5, but they are unimportant for the trends with environment, because we always study environmental effects at fixed redshift, and we see no significant dependence of galaxy size on environment. We have

also corrected all line indices for the effects of velocity dispersion calibrated using the Bruzual & Charlot (2003) models and assuming Gaussian velocity distributions. In principle, the correction is different for non-Gaussian velocity distributions (e.g., Kuntschner 2004); we have chosen the Gaussian because our analysis is based on composite spectra, so choosing the appropriate non-Gaussian model to make the correction is not straightforward.

Tables 2–4 give our measurements of the index strengths in these composite spectra. In § 6 we use stellar population synthesis models to interpret these measurements. These assume measurements at Lick rather than SDSS resolution, so, in that section only, we smooth the spectra to Lick resolution before correcting for the effects of velocity dispersion. The line strengths at Lick resolution for the indices used in that section are given in Table 7.

3. THE FUNDAMENTAL PLANE

There are a number of small but significant differences between our early-type galaxy samples in low- and high-density environments. A traditional way to search for trends with environment is to study the distribution of galaxies in the space of $\log(\text{size})$, $\log(\text{velocity dispersion})$, and $\log(\text{surface brightness})$. In this space, early-type galaxies populate a Fundamental Plane (e.g., Dressler et al. 1987; Djorgovski & Davis 1987). The solid line in the top panel of Figure 3 shows the best *orthogonal fit* (determined following the methods described in Bernardi et al. [2003c]) Fundamental Plane in the r band using all early-type galaxies in our sample, whatever their environment. (Although the old photometric reductions output by the SDSS pipeline PHOTO were incorrect, using the new corrected photometry has not significantly changed the coefficients of the Fundamental Plane from those reported in Bernardi et al. [2003c].) The dashed contours show the distribution of the subset of cluster galaxies in dense regions around the plane, while the dotted contours represent galaxies in less dense regions. The dependence

TABLE 2
LINE STRENGTHS AND UNCERTAINTIES MEASURED FROM THE COMPOSITE SPECTRA GIVEN IN TABLE 1

ID	O II (Å)	Err (Å)	H δ_A (Å)	Err (Å)	H δ_F (Å)	Err (Å)	H γ_A (Å)	Err (Å)	H γ_F (Å)	Err (Å)	D4000	Err
1.....	-1.036	0.530	-1.579	0.420	0.304	0.296	-4.967	0.357	-0.723	0.231	1.902	0.018
2.....	-1.446	0.484	-1.996	0.362	0.362	0.247	-4.791	0.291	-1.260	0.191	1.865	0.015
3.....	-0.210	0.484	-1.919	0.423	0.477	0.286	-6.164	0.358	-1.873	0.239	1.890	0.017
4.....	-1.638	0.384	-2.739	0.265	0.699	0.190	-5.673	0.222	-1.817	0.142	1.963	0.013
5.....	0.518	0.352	-2.508	0.277	0.120	0.201	-6.861	0.243	-2.527	0.170	1.956	0.012

NOTES.—Table 2 is published in its entirety in the electronic edition of the *Astronomical Journal*. A portion is shown here for guidance regarding its form and content.

on environment is weak. To show the dependence more clearly, the inset shows the distribution of residuals from the plane: evidently, galaxies in dense regions tend to have slightly (0.075 ± 0.008 mag) fainter surface brightnesses than their counterparts in less dense regions. The bottom panel shows a similar analysis of Fundamental Plane residuals in the g and i bands, for which the shifts are 0.081 ± 0.008 and 0.069 ± 0.007 mag, respectively. Note that the typical scatter around the plane is not significantly smaller in the cluster sample than in the low-density sample. (Table 5 gives the mean offsets in each band for the two environments, as well as the rms residual.)

Our findings are consistent with a model in which the stars in any given early-type galaxy formed in a single burst and, for the galaxies that are now in dense regions, in which this burst happened at higher redshifts. But a model in which the chemical abundances (e.g., metallicities) depend on environment would also work. In § 6 we use single-burst stellar population synthesis models to interpret these trends in terms of age and/or metallicity differences between the two populations. A more model-independent analysis is the subject of § 5.

4. ADDITIONAL TRENDS WITH ENVIRONMENT

This section studies how various structural parameters and chemical abundance indicators depend on environment. In the figures that follow, we often group together observables that are expected to trace similar physics. To facilitate comparison of different observables with one another, we standardize as follows: for each observable Y we compute the mean $\langle Y \rangle$ and the rms simply by summing over the entire sample of composite spectra, weighting each by the number of galaxies in the composite. We then show $(Y - \langle Y \rangle)/\text{rms}(Y)$, rather than Y itself. To simplify interpretation of selection effects, we show results from subsamples in different redshift bins. The values of $\langle Y \rangle$ and $\text{rms}(Y)$ are provided in Table 6.

The mean and rms values we quote are obtained by number weighting the composites when averaging, rather than averaging over the galaxies themselves. We have chosen to do this because line strengths computed from individual rather than composite spectra are very unreliable, so for most choices of Y we must use composites. Therefore, although the mean values we quote should be accurate, the quoted rms values may underestimate the true scatter because they do not include the contribution from the scatter among objects that make up each composite. However, because our composites are constructed from sufficiently small bins in the parameters that correlate most strongly with index strengths, it is likely that the scatter within a bin is negligible compared to the scatter between bins.

As a check, we performed all the analysis that follows using individual rather than composite spectra, subtracting the measurement errors in quadrature when computing rms values. This

showed that our quoted rms values actually do not underestimate the true scatter substantially. Using the individual spectra rather than the composites has no effect on any of our qualitative conclusions, but because quantitative measurements based on composites are more robust, we have chosen to present all results using the composites only.

Note that a variety of emission and absorption lines, as well as the Lick indices, are known to correlate with luminosity and/or velocity dispersion. We have measured a number of such correlations (for a selection, see Bernardi et al. [2003d] as well as Appendix B): for most, the primary correlation is with velocity dispersion, the correlation with luminosity (if present) being primarily a consequence of the index- σ and luminosity- σ correlations. In this respect, many line strengths behave similarly to color (Bernardi et al. 2003d, 2005). Therefore, if we find that these line strengths vary with environment, it is important to check whether the environmental trend is entirely a consequence of a correlation between luminosity and/or velocity dispersion and environment, or whether the environment did indeed play an additional role.

4.1. Structural Parameters

Since we are interested in whether or not environment plays a role over and above determining the structural parameters of galaxies, Figure 4 shows the typical values of luminosity, velocity dispersion, mass, size, color, and light-profile shape fracDev in dense and less dense regions. All observables have been rescaled by subtracting the mean in the entire sample and then dividing by the rms. The x -axis lists the observable and the value of the rms. Solid and dashed lines show the median values in dense and less dense regions, respectively. Error bars show the error on this median value, and shaded regions show the 25% and 75% values. (An asterisk signifies that the quoted rms is for the logarithm of the index.) To simplify interpretation of selection effects, we show results from subsamples at $0.05 < z < 0.07$, $0.07 \leq z < 0.09$, $0.09 \leq z < 0.12$, and $0.12 \leq z < 0.14$. The text in the top right of each panel indicates the total number of composites in each redshift bin and the total number of galaxies that made up those composites.

Note that the supercluster at $z \sim 0.08$ is obvious: the ratio of the number of galaxies in high-density regions to that in regions of lower density is considerably higher in the $0.07 < z < 0.09$ bin. In what follows, we see some peculiarities in this redshift bin.

The main point of this figure is not to compare the different panels with one another but to compare the two environments in each panel with one another. This is because the primary difference between the different panels is caused by the magnitude limit: the higher redshift samples contain objects that are more luminous, have higher velocity dispersions, and have larger

TABLE 3
LICK INDEX STRENGTHS AND UNCERTAINTIES MEASURED FROM THE COMPOSITE SPECTRA GIVEN IN TABLE 1

ID	CN ₁ (mag)	Err	CN ₂ (mag)	Err	Ca4227 (Å)	Err	G4300 (Å)	Err	Fe4383 (Å)	Err	Ca4455 (Å)	Err	Fe4531 (Å)	Err	C ₂ 4668 (Å)	Err	Hβ (Å)	Err	Fe5015 (Å)	Err
1.....	0.092	0.011	0.141	0.011	1.758	0.185	5.974	0.289	6.733	0.306	2.572	0.199	4.561	0.241	6.346	0.309	1.983	0.164	5.959	0.271
2.....	0.095	0.009	0.123	0.009	1.094	0.161	5.747	0.254	6.022	0.259	2.407	0.166	3.872	0.206	6.102	0.271	2.075	0.144	6.120	0.226
3.....	0.146	0.012	0.201	0.012	1.347	0.203	6.044	0.305	5.452	0.340	1.756	0.193	4.144	0.277	6.264	0.353	1.326	0.192	6.071	0.298
4.....	0.120	0.007	0.173	0.007	1.583	0.118	6.248	0.200	5.883	0.199	2.086	0.115	3.723	0.149	7.037	0.189	1.664	0.114	6.181	0.166
5.....	0.126	0.008	0.171	0.008	1.384	0.117	6.693	0.185	6.066	0.203	2.188	0.118	4.735	0.158	6.668	0.205	1.654	0.109	4.713	0.190

NOTES.—Table 3 is published in its entirety in the electronic edition of the *Astronomical Journal*. A portion is shown here for guidance regarding its form and content.

TABLE 4
ADDITIONAL LICK INDEX STRENGTHS AND UNCERTAINTIES MEASURED FROM THE COMPOSITE SPECTRA GIVEN IN TABLE 1

ID	Mg ₁ (mag)	Err	Mg ₂ (mag)	Err	Mg <i>b</i> (Å)	Err	Fe5270 (Å)	Err	Fe5335 (Å)	Err	Fe5406 (Å)	Err	Fe5709 (Å)	Err	Fe5782 (Å)	Err	NaD (Å)	Err	TiO ₁ (mag)	Err	TiO ₂ (mag)	Err
1.....	0.137	0.004	0.256	0.006	3.702	0.186	3.613	0.361	2.543	0.193	2.071	0.156	1.365	0.118	1.367	0.102	3.104	0.140	0.052	0.005	0.095	0.003
2.....	0.123	0.004	0.253	0.005	4.415	0.158	2.781	0.297	2.871	0.170	2.220	0.137	1.168	0.117	0.774	0.090	3.036	0.124	0.045	0.003	0.082	0.002
3.....	0.149	0.005	0.284	0.007	4.711	0.209	3.308	0.307	2.340	0.209	1.874	0.186	1.132	0.129	1.182	0.117	3.678	0.175	0.038	0.004	0.086	0.003
4.....	0.144	0.003	0.287	0.003	4.656	0.108	3.879	0.164	3.115	0.109	2.200	0.094	1.301	0.071	1.015	0.062	3.908	0.092	0.047	0.002	0.090	0.001
5.....	0.154	0.003	0.291	0.004	4.429	0.128	3.440	0.172	3.512	0.119	2.055	0.106	0.885	0.077	1.024	0.068	3.983	0.093	0.050	0.003	0.092	0.002

NOTES.—Table 4 is published in its entirety in the electronic edition of the *Astronomical Journal*. A portion is shown here for guidance regarding its form and content.

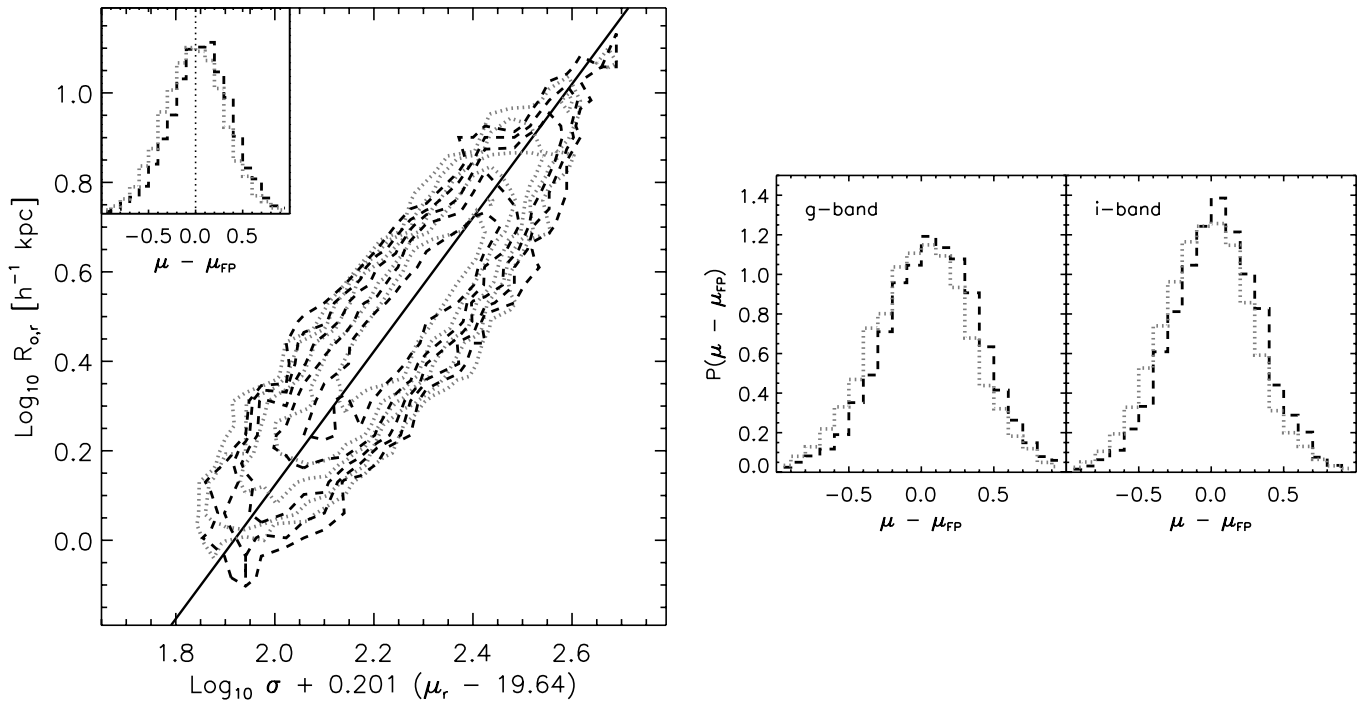


FIG. 3.—*Left*: Fundamental Plane in the r band. The solid line shows the fit from Bernardi et al. (2003c). The dashed and dotted lines represent the subset of galaxies that populate dense and less dense regions, respectively. The inset shows the distribution of residuals in surface brightness: galaxies in dense regions tend to be ~ 0.08 mag fainter than those in the least dense regions. *Right*: Distribution of residuals in surface brightness with respect to the Fundamental Plane in the g and i bands. The offset between low-density and high-density samples is similar to that in the r band. Note that the width of the distribution of residuals is approximately independent of environment.

masses and sizes. However, the figure shows that, in any given redshift bin, trends with environment are weak: in all cases in which there is a small difference, the objects in the low-density environments tend to be slightly less luminous, to have smaller velocity dispersions, masses, and sizes, and to be slightly bluer, although these differences are usually less than 20% of the rms variation across the entire sample (i.e., two tick marks), except in the highest redshift bin.

To remove the effects of correlations with luminosity or velocity dispersion, we have further divided each redshift bin into narrow bins in luminosity. Figure 5 shows that the small environmental trends evident in Figure 4 are seen consistently in all the panels. The top two panels of Figure 5 show the values of the structural parameters of galaxies that are slightly more luminous than L_* : in the lowest redshift bin (*top left*), the luminosities, velocity dispersions, masses, sizes, and profile shapes (fracDev) of the high- and low-density environment samples are virtually identical, whereas a small but significant difference is detected in the color. Except for the color, the panel on the top right shows similar trends, but recall that this redshift bin contains a supercluster, and this may bias our results.

TABLE 5

DEPENDENCE OF MEAN AND RMS RESIDUALS FROM THE FUNDAMENTAL PLANE ON ENVIRONMENT

Band	$\langle \Delta\mu \rangle_{\text{high}}$ (mag)	$\langle \Delta\mu \rangle_{\text{low}}$ (mag)	$\text{rms}(\Delta\mu)_{\text{high}}$ (mag)	$\text{rms}(\Delta\mu)_{\text{low}}$ (mag)
g	0.075 ± 0.006	-0.006 ± 0.005	0.345	0.355
r	0.055 ± 0.006	-0.020 ± 0.005	0.328	0.335
i	0.034 ± 0.006	-0.035 ± 0.004	0.324	0.322

NOTE.—Computed using the coefficients of the orthogonal fit, in different bands.

The bottom two panels show results in the two higher redshift bins, for which the bin in luminosity is necessarily brighter. In these panels the sample in low-density regions is significantly bluer, even though the median luminosity and velocity dispersion are the same as that in the higher density sample (this is not quite true for the bottom right panel, in which σ seems to scatter to smaller values in lower density regions). This illustrates clearly that the environment plays a role in determining galaxy colors. A Kolmogorov-Smirnov (K-S) test confirms what is obvious to the eye: the only cases in which the distributions of the parameters in low- and high-density regions are significantly different ($p_{\text{KS}} < 0.05$) are for the $g-r$ color in the top left and bottom two panels.

The trends in Figure 5 are reported in Table 6. Comparison of the two values of fracDev in each panel of this figure and Figure 4 (also see Table 6) show that the mean fracDev is the same in both dense and less dense regions. (We do not expect fracDev to distinguish between S0 and elliptical galaxies; for our purposes, S0 and elliptical galaxies are both early types.) Since fracDev is an indicator of morphology, this shows that any trends with environment are probably *not* driven by a correlation between morphology and density (e.g., Dressler 1980). If some of the trends we see are indeed associated with the morphology-density relation, then the differences we detect in the properties of galaxies in high- and low-density regions are overestimates of the true differences. This places even tighter limits on the possible role played by the environment.

4.2. O II, Balmer Lines, D4000, and α -Elements

This subsection studies the correlation between emission-line strengths (O II), absorption lines that are not part of the original Lick system (Worthey et al. 1994; Trager et al. 1998), i.e., the Balmer line indices H δ and H γ (Worthey & Ottaviani

TABLE 6
COMPARISON OF EVOLUTION AND ENVIRONMENT SHOWN IN FIGURES 8–10

Parameter	$\langle Y \rangle$	rms(Y)	$\Delta Y(\text{Dens})\text{-I}$	$\Delta Y(\text{Dens})\text{-II}$	$\Delta Y(\text{Dens})\text{-III}$	$\Delta Y(\text{Dens})\text{-IV}$	$\Delta Y(\text{Evol})$
M_r (mag)	-21.91	0.71	0.054 ± 0.038	0.027 ± 0.033	0.087 ± 0.035	-0.021 ± 0.047	0.091 ± 0.028
σ (km s $^{-1}$)	2.26	0.10	0.001 ± 0.011	-0.001 ± 0.010	0.002 ± 0.010	0.015 ± 0.010	0.007 ± 0.009
$*R_{o,r}\sigma^2$	5.02	0.35	0.011 ± 0.027	0.071 ± 0.023	-0.003 ± 0.023	0.049 ± 0.026	-0.017 ± 0.021
$*R_{o,r}$ (kpc h $^{-1}$)	0.49	0.23	0.004 ± 0.021	0.024 ± 0.019	0.026 ± 0.020	0.006 ± 0.021	-0.011 ± 0.017
$g-r$ (mag)	0.73	0.04	0.016 ± 0.005	0.003 ± 0.004	0.024 ± 0.005	0.032 ± 0.006	0.031 ± 0.004
fracDev	0.96	0.04	-0.003 ± 0.006	-0.004 ± 0.004	-0.002 ± 0.007	0.006 ± 0.007	0.006 ± 0.004
O II (\AA)	2.29	1.52	-0.757 ± 0.128	-0.759 ± 0.117	-0.793 ± 0.151	-0.469 ± 0.166	-0.702 ± 0.119
H δ_A (\AA)	-1.72	0.93	-0.358 ± 0.111	-0.263 ± 0.080	-0.373 ± 0.103	-0.421 ± 0.135	-0.372 ± 0.073^a
H δ_F (\AA)	0.66	0.46	-0.077 ± 0.062	-0.131 ± 0.038	-0.057 ± 0.049	-0.092 ± 0.066	-0.146 ± 0.035^a
H γ_A (\AA)	-5.37	0.85	-0.287 ± 0.110	-0.280 ± 0.082	-0.432 ± 0.085	-0.399 ± 0.117	-0.235 ± 0.064^a
H γ_F (\AA)	-1.41	0.54	-0.226 ± 0.071	-0.138 ± 0.051	-0.275 ± 0.051	-0.150 ± 0.070	-0.118 ± 0.040^a
D4000	1.90	0.08	0.024 ± 0.009	0.026 ± 0.007	0.028 ± 0.008	0.036 ± 0.010	0.035 ± 0.007^a
$*[\text{MgFe}]'$	0.58	0.04	0.021 ± 0.005	0.008 ± 0.004	0.009 ± 0.004	0.017 ± 0.006	0.011 ± 0.003
$*\text{Mg } b/\langle\text{Fe}\rangle$	0.13	0.05	0.024 ± 0.005	0.003 ± 0.004	0.003 ± 0.005	0.012 ± 0.007	0.012 ± 0.003
CN $_1$	0.11	0.03	0.010 ± 0.004	0.002 ± 0.003	0.009 ± 0.004	0.010 ± 0.004	0.010 ± 0.004^a
CN $_2$ (mag)	0.16	0.04	0.018 ± 0.005	-0.002 ± 0.004	0.018 ± 0.005	0.017 ± 0.006	0.010 ± 0.004^a
$*\text{Ca}4227$ (\AA)	0.19	0.06	0.026 ± 0.007	-0.001 ± 0.006	0.007 ± 0.007	0.019 ± 0.007	0.011 ± 0.004^a
$*\text{G}4300$ (\AA)	0.77	0.03	0.010 ± 0.003	0.003 ± 0.003	0.008 ± 0.003	0.013 ± 0.005	0.006 ± 0.002^a
$*\text{Fe}4383$ (\AA)	0.76	0.05	0.017 ± 0.005	0.009 ± 0.005	-0.014 ± 0.005	0.009 ± 0.007	0.010 ± 0.003
$*\text{Ca}4455$ (\AA)	0.33	0.07	0.021 ± 0.007	0.020 ± 0.006	-0.001 ± 0.008	0.005 ± 0.010	0.005 ± 0.005
$*\text{Fe}4531$ (\AA)	0.61	0.04	-0.002 ± 0.004	-0.001 ± 0.004	-0.003 ± 0.004	-0.006 ± 0.005	0.004 ± 0.002
$*\text{C}24668$ (\AA)	0.85	0.06	-0.003 ± 0.007	-0.002 ± 0.006	0.021 ± 0.007	0.006 ± 0.008	0.036 ± 0.005
$*\text{H}\beta$ (\AA)	0.25	0.07	-0.005 ± 0.008	0.002 ± 0.007	-0.010 ± 0.008	-0.010 ± 0.009	-0.013 ± 0.005
$*\text{Fe}5015$ (\AA)	0.77	0.05	0.007 ± 0.005	0.009 ± 0.004	0.020 ± 0.006	0.014 ± 0.007	-0.002 ± 0.003
Mg $_1$ (mag)	0.14	0.02	0.009 ± 0.003	0.004 ± 0.002	0.006 ± 0.002	0.011 ± 0.002	0.010 ± 0.002
Mg $_2$ (mag)	0.27	0.03	0.015 ± 0.004	0.007 ± 0.003	0.014 ± 0.004	0.011 ± 0.004	0.017 ± 0.003
$*\text{Mg } b$ (\AA)	0.64	0.06	0.026 ± 0.007	0.020 ± 0.006	0.026 ± 0.006	0.016 ± 0.009	0.023 ± 0.005
$*\text{Fe}5270$ (\AA)	0.52	0.05	0.003 ± 0.005	0.005 ± 0.004	-0.004 ± 0.005	0.009 ± 0.007	0.005 ± 0.003
$*\text{Fe}5335$ (\AA)	0.50	0.06	0.005 ± 0.006	0.004 ± 0.006	0.007 ± 0.007	0.020 ± 0.008	0.004 ± 0.003
$*\text{Fe}5406$ (\AA)	0.31	0.06	0.006 ± 0.006	0.009 ± 0.005	-0.004 ± 0.006	0.001 ± 0.009	0.005 ± 0.003
$*\text{Fe}5709$ (\AA)	0.03	0.07	0.000 ± 0.006	0.001 ± 0.007	-0.011 ± 0.009	-0.018 ± 0.009	-0.015 ± 0.004
$*\text{Fe}5782$ (\AA)	-0.02	0.09	0.019 ± 0.009	0.008 ± 0.008	-0.023 ± 0.009	-0.011 ± 0.016	0.012 ± 0.005
$*\text{NaD}$ (\AA)	0.60	0.08	0.009 ± 0.009	0.002 ± 0.008	-0.005 ± 0.008	0.026 ± 0.009	0.049 ± 0.007
TiO $_1$ (mag)	0.04	0.01	0.003 ± 0.001	-0.003 ± 0.001	0.001 ± 0.001	0.003 ± 0.001	0.002 ± 0.001
TiO $_2$ (mag)	0.08	0.01	0.002 ± 0.001	0.004 ± 0.001	0.002 ± 0.001	0.002 ± 0.001	0.004 ± 0.001

NOTES.—The first column shows the name of the observable; if preceded by an asterisk, then Y in subsequent columns is obtained from the logarithm of the observable, $\langle Y \rangle$ is the (number-weighted) mean of Y over the sample of composites, and rms(Y) is the rms spread around this mean. Both the mean and rms are obtained by summing over composite spectra, weighting each by the number of galaxies in it. The quantities $\Delta Y(\text{dens}) = Y(\text{high dens}) - Y(\text{low dens})$. Roman numerals I and II are for galaxies with $-22 \leq M_i \leq -21$ in redshift bins $0.05 < z < 0.07$ and $0.07 < z < 0.09$, respectively. Roman numerals III and IV are for galaxies with $-23 \leq M_i \leq -22$ in redshift bins $0.09 < z < 0.12$ and $0.12 < z < 0.14$, respectively. The final column shows $\Delta Y(\text{evol}) = Y(z \sim 0.06) - Y(z \sim 0.17)$ for galaxies with $2.35 \leq \log \sigma \leq 2.4$.

^a Reported value has been corrected for flux calibration problems by dividing the observed value by a factor of 3 (see Appendix B).

1997), the strength D4000 of the break in the spectrum at 4000 \AA (e.g., Balogh et al. 1999), and some combinations of the Mg and Fe lines, i.e., $[\text{MgFe}]'$ (e.g., TMB03) and $\text{Mg}/\langle\text{Fe}\rangle$, with the environment. The O II emission line is an indicator either of very recent star formation or of AGN activity, the Balmer (absorption) line indices are sensitive to star formation, the 4000 \AA break is an indicator of age (although all these observables also depend on metallicity and α -element abundance ratios of the stellar population), $\text{Mg}/\langle\text{Fe}\rangle$ is an indicator of the α -element abundance ratios (in early-type galaxies, this ratio is enhanced relative to the solar value), and $[\text{MgFe}]'$ is an index that is an indicator of metallicity that is not expected to be very sensitive to the α -element abundance ratios.

To simplify interpretation of the results, Figure 6 presents measurements in the same narrow bins in redshift and luminosity as were used in Figure 5. Recall that, for these bins, the effects of correlations between luminosity, velocity dispersion, and environment are unimportant. (Plots similar to Fig. 4 show similar trends to those in Fig. 6 but are more difficult to interpret.) Galaxies in low-density regions have stronger emission lines,

stronger Balmer lines, and weaker 4000 \AA breaks. They also tend to have lower values of $[\text{MgFe}]'$ and $\text{Mg}/\langle\text{Fe}\rangle$. (K-S tests indicate that the distributions are not significantly different if the small error bars shown for each parameter overlap.) In all observables, the high- and low-density samples differ by about three tick marks, indicating that the difference is about 30% of the rms spread across the entire sample. Table 6 gives more precise values for these differences.

Recall that the mean luminosities and velocity dispersions are the same in dense and less dense environments. Therefore, trends with environment in Figure 6 are *not* the result of index- σ and σ -environment correlations. We have already argued that these trends are probably not due to the morphology-density relation either.

4.3. Lick Indices

Lick indices (defined as in Trager et al. 1998) for objects with the same narrow range of redshifts and luminosities as in Figure 6 are shown in Figure 7. The indices are arranged in order of increasing wavelength, so the figure can be thought of

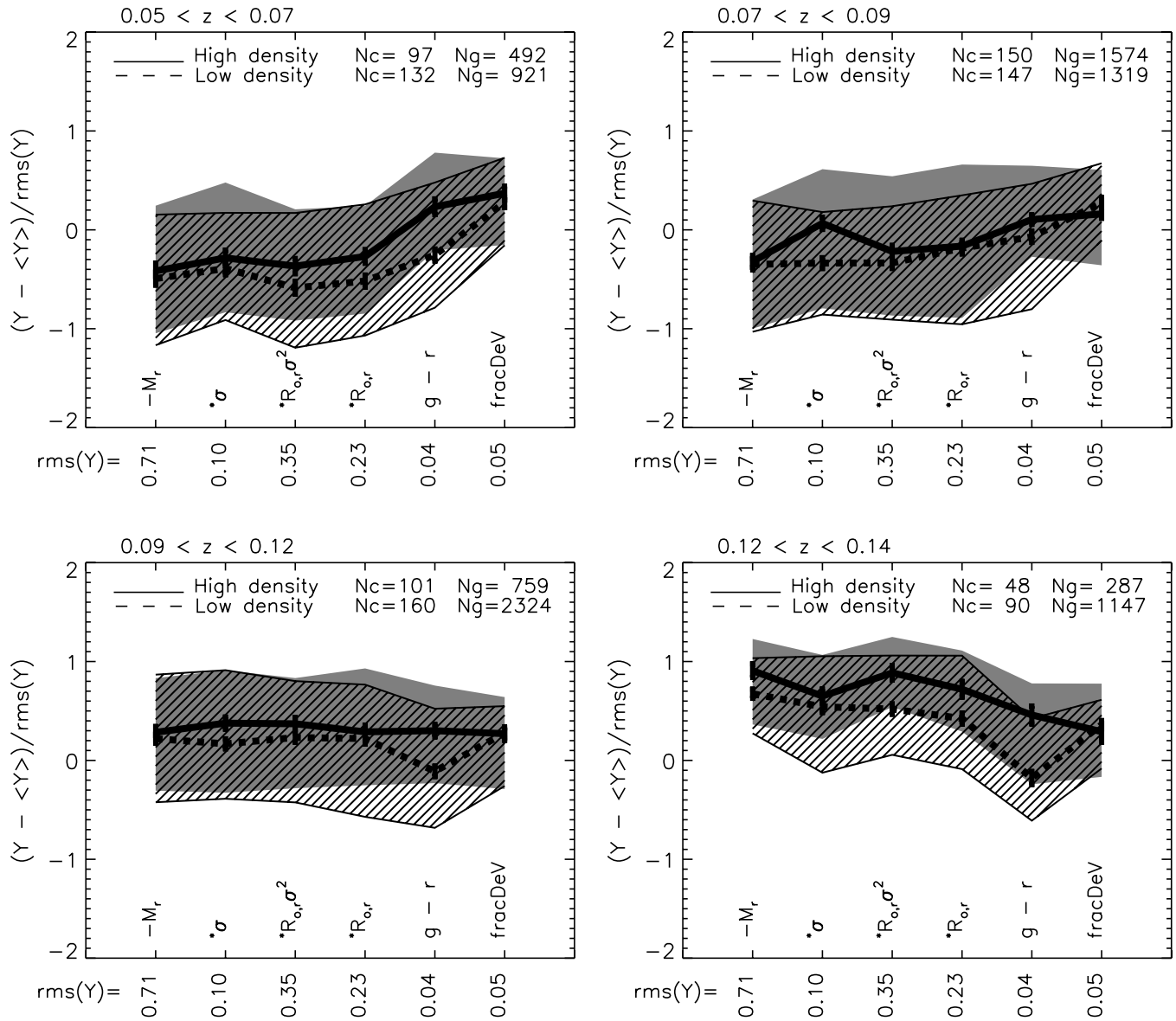


FIG. 4.—Median values of luminosity, velocity dispersion, mass, size, color, and light-profile shape fracDev (i.e., morphological type) in dense and underdense regions. To facilitate comparison with one another, all observables have been rescaled by subtracting the mean and then dividing by the rms spread across the entire sample (i.e., across all redshifts and luminosities). The x-axis lists the observable and the value of the rms. An asterisk denotes that the quoted rms is for the logarithm of the parameter. Shaded regions show the 25% and 75% values. Different panels show subsamples at $0.05 < z < 0.07$, $0.07 \leq z < 0.09$, $0.09 \leq z < 0.12$, and $0.12 \leq z < 0.14$. The text in the top right of each panel indicates the total number of composites in each redshift bin and the total number of galaxies that made up those composites. The top right panel contains a supercluster, so environmental effects may not be accurate.

as illustrating how (little) the spectrum depends on environment. Note that the Mg line strengths tend to be slightly weaker in the low-density regions (about 30% of the rms across the full sample, making Mg_2 and $\text{Mg } b$ weaker by about 0.01 ± 0.004 mag and 0.2 ± 0.06 Å, respectively). On the other hand, most of the Fe indicators show no significant dependence on environment. Once again, K-S tests indicate that the error bars provide a reasonably accurate guide to the significance of the difference between environments: overlapping error bars indicate no significant difference.

Table 6 quantifies the trends we have detected; recall that they are *not* the result of index- σ and σ -environment correlations and that they are unlikely to have arisen from a morphology-density relation. Presumably, age, metallicity, and α -element abundance differences play some role in the dependence on environment. By studying which indices behave similarly in

these plots, one can begin to identify which elements respond similarly to variations in age, metallicity, and α -abundance. We discuss this in § 5.

5. EVOLUTION AND ENVIRONMENT

Section 4 showed that, at any given redshift, many line strengths depend weakly but significantly on environment. On the other hand, many of the line strengths have evolved significantly between $z = 0.05$ and 0.15 (Bernardi et al. 2003d). Section 6 uses stellar population synthesis models to interpret our measurements. This section describes a relatively model-independent interpretation of what our measurements mean.

5.1. Measurements of Evolution

The luminosity function of this sample changes slightly with redshift (Bernardi et al. 2003b). The observed evolution can be

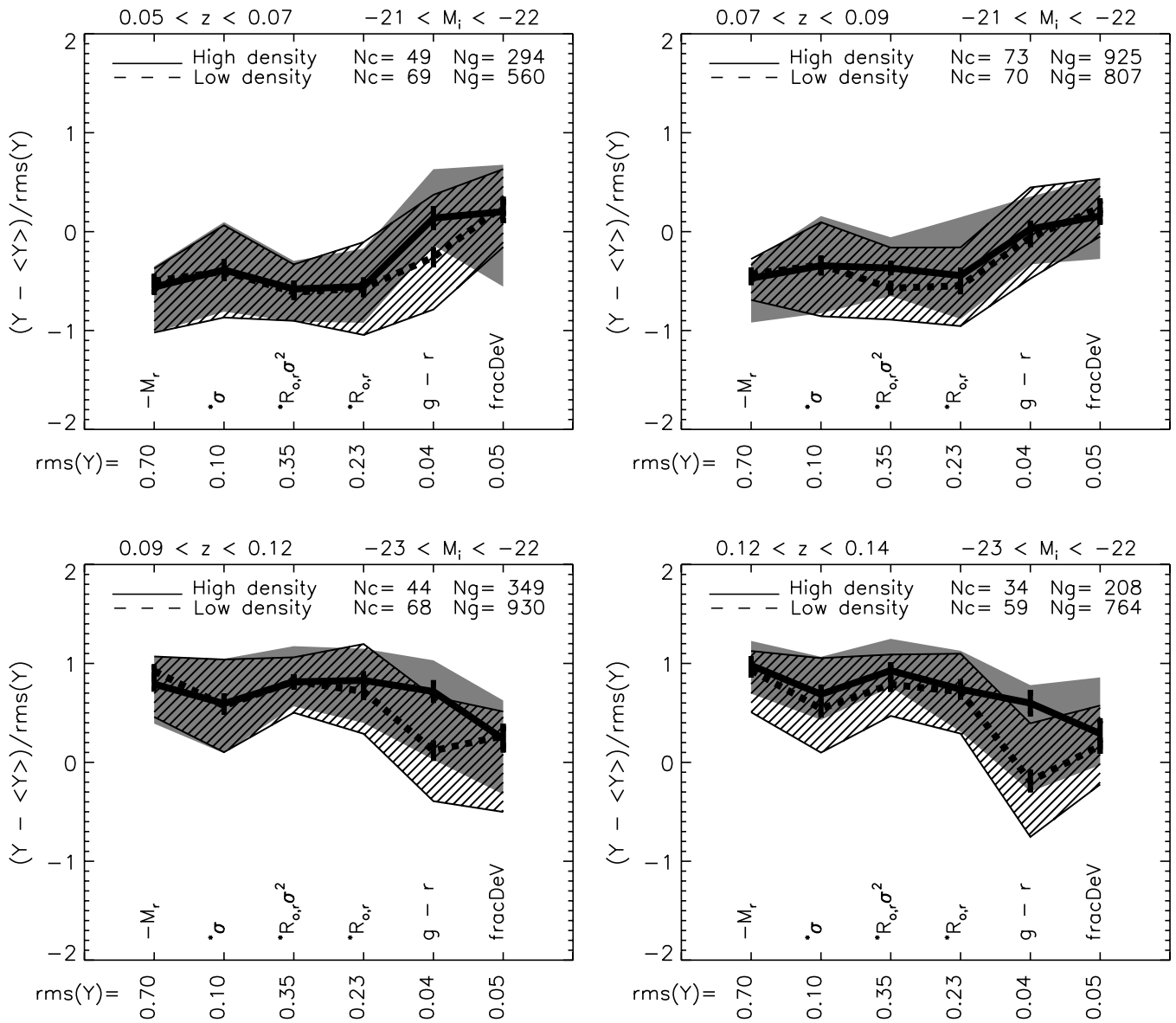


FIG. 5.—As in Fig. 4, but only for results from objects with a narrow range of luminosities (indicated in the top right of each panel). The magnitude limit of the sample means that the low-redshift bins contain objects with smaller luminosities than the higher redshift bins. (An asterisk signifies that the quoted rms is for the logarithm of the index.) In these narrow bins of redshift and luminosity, the mean velocity dispersions are similar in dense and less dense environments (this is not quite true for the bottom right panel, in which σ seems to scatter to smaller values in lower density regions). The top right panel is different from the others; it happens to contain a supercluster, and this may have compromised our estimates of environmental effects.

accounted for if one assumes that the number densities are not changing but that the higher redshift population is more luminous than that at lower redshifts: the change is $1.15z$, $0.85z$, and $0.75z$ in the g , r , and i bands, respectively. Since a pure luminosity evolution model is consistent with the data, it is plausible that the population at lower redshifts is a passively evolved sample of the population at higher redshifts. If so, then the observed evolution with redshift can be used as a clock. The argument is as follows.

The dashed lines in Figures 8–10 show how the structural parameters and line strengths vary as the redshift changes. These dashed lines (the same in all four panels of each figure) represent the evolution of galaxies with $2.35 \leq \log \sigma \leq 2.4$ over the redshift range $0.06 \leq z \leq 0.17$. The actual values are reported in Table 6. (The redshift limits were set by requiring that these objects be seen over the entire redshift range, so as to minimize selection effects. Appendix A discusses why selection effects are

important, why we chose this bin in σ , and why our estimates of evolution are almost certainly upper limits.)

By using the same dashed curve in all four panels (note that the solid curves in the top two panels in each figure are for a lower luminosity bin), we are implicitly assuming that evolution is not differential (i.e., all galaxies evolve similarly). Since age is likely the main driver for the dependence on redshift, indices with similar values traced by the dashed line may have a similar fraction of the total scatter across the whole sample arising from changes in age. For reference, the range $0.06 \leq z \leq 0.17$ corresponds to a time interval of ~ 1.3 Gyr.

Before we consider these figures in detail, recall that the Fundamental Plane indicates that galaxies in cluster-like environments are fainter than their counterparts in less dense regions (see Table 5). Pure luminosity evolution for $0.06 \leq z \leq 0.17$ gives approximately the same shift in magnitudes as those listed in Table 5 (e.g., in the r band, the difference between

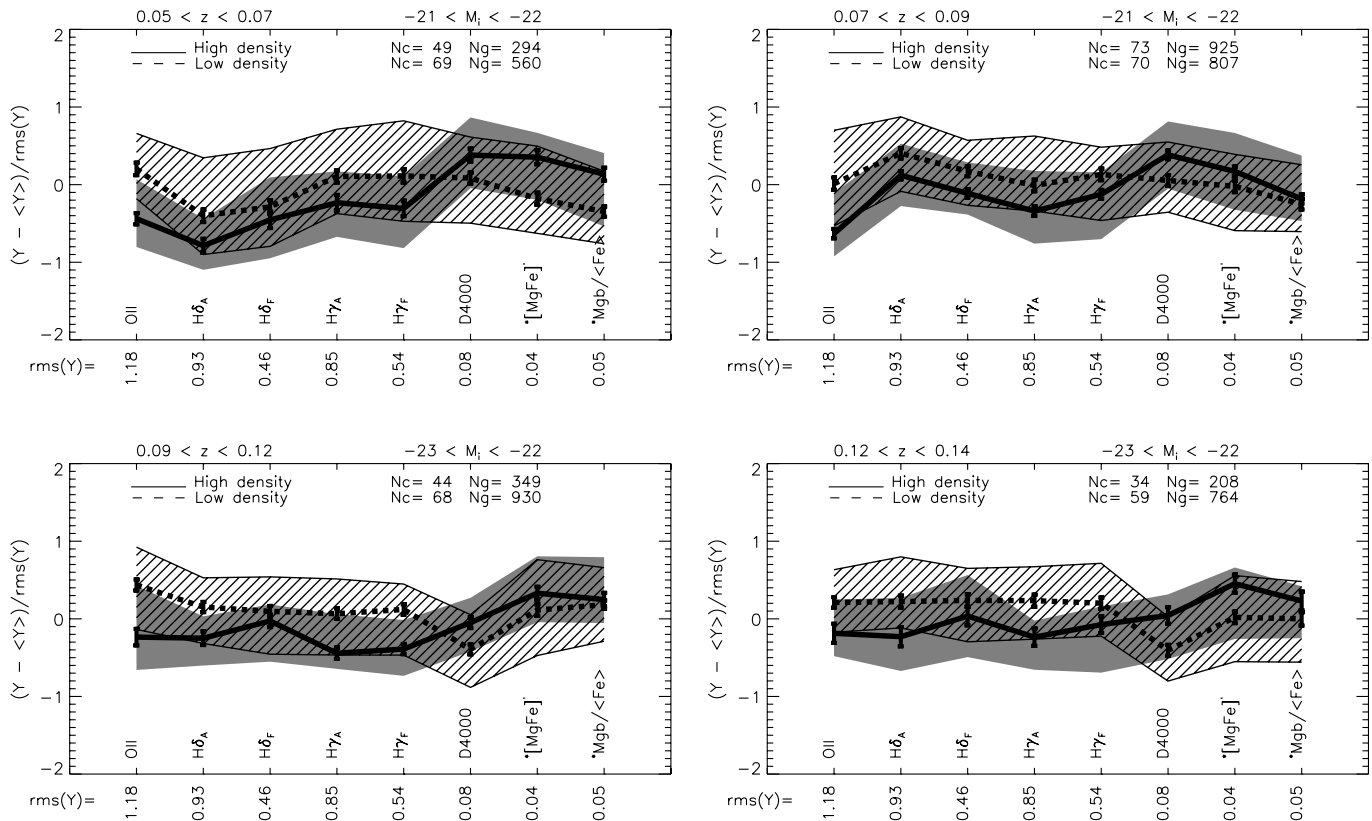


FIG. 6.—Emission-line strengths (O II), star formation indicators (H δ , H γ), the strength of the break at 4000 Å (D4000), and the combinations [MgFe]' and Mg/⟨Fe⟩ for objects with the same narrow range of redshifts and luminosities as in Fig. 5. An asterisk signifies that the quoted rms is for the logarithm of the index.

environments is ~ 0.08 mag, and the evolution is $0.85\Delta z \sim 0.09$ mag). If the difference between the two environments is entirely due to age effects, then the objects in cluster-like environments must be older by 1.3 Gyr. If the other structural parameters and line strengths show environmental differences similar to those seen by comparing populations at redshifts separated by 1.3 Gyr, then this would constrain the roles played by age and metallicity in determining environmental differences.

Figure 8 indicates that color is different from the other parameters such as size and velocity dispersion: 1.3 Gyr of evolution appear to account for the entire spread in color values but accounts for a negligible fraction of the spread in velocity dispersions, sizes, and masses. Evidently, color responds very differently to age than do the other parameters. We discuss this in more detail shortly.

The dashed lines in Figure 9 indicate that the Balmer lines are weaker at low redshift, whereas D4000, [MgFe]', and Mg/⟨Fe⟩ are slightly stronger. The sign of the evolution is consistent with that of an aging single-burst population. Taken at face value, Figure 9 indicates that an age difference of 1.3 Gyr can produce a change in the Balmer line strengths and in D4000 that is almost as large as the rms spread across the whole sample. However, this apparently dramatic evolution should be treated cautiously. At low redshifts, the Balmer lines and D4000 are close to the edge of the SDSS spectrograph, where there are known to be flux calibration problems at the 3% level. Evidence that this may have compromised our estimates of evolution is presented in Appendix B: the apparent evolution of $H\delta_A + H\gamma_A$ is about 3 times larger than measurements from the literature suggest (Kelson et al. 2001). Hence, the dotted lines in Figure 9 show the result of dividing all estimates of evolution for the Balmer lines and D4000 by a factor of 3. When this is done, 1.3 Gyr of evolution produces a similar

fraction of the rms spread ($\sim 30\%$) for O II, [MgFe]', and Mg/⟨Fe⟩. Note that this is a smaller fraction of the rms spread than it was for color.

The dashed lines in Figure 10 show that evolution accounts for different fractions of the rms spread across the sample for the different Lick indices. (We have again corrected for potential flux calibration problems by reducing the measured values, for indices with rest wavelengths shorter than 4350 Å, by a factor of 3: the dotted curves show these corrected values.) For instance, an age difference of 1.3 Gyr produces a change in Mg that is 50% of the spread in Mg line strengths. If the spread in ages across the sample is 1.3 Gyr, as color indicates, then we must conclude that other effects (such as metallicity) are responsible for the remaining scatter. Similarly, evolution changes the Fe index strengths by a negligible fraction of the spread in Fe index values (typically about 0.06 dex). Evidently, this spread must be due to effects other than (or in addition to) age. In this respect, our results indicate that Fe and Mg respond differently to age and metallicity and that C₂4668 and NaD are more similar to Mg than to Fe.

Note that H β appears to evolve slightly less than the other Balmer lines shown in Figure 9. Although it is more sensitive to fill-in by emission than the other Balmer lines, we have attempted to correct for this (recall we add 0.05 times the O II line to the measured value). Since emission is more likely in the higher redshift population, it may be that the deepening of the H β absorption feature with redshift is compensated by fill-in due to emission, and our correction has not completely accounted for this.

5.2. Dependence on Environment

The solid lines in Figures 8–10 show variations with environment. Each panel shows environmental differences for galaxies

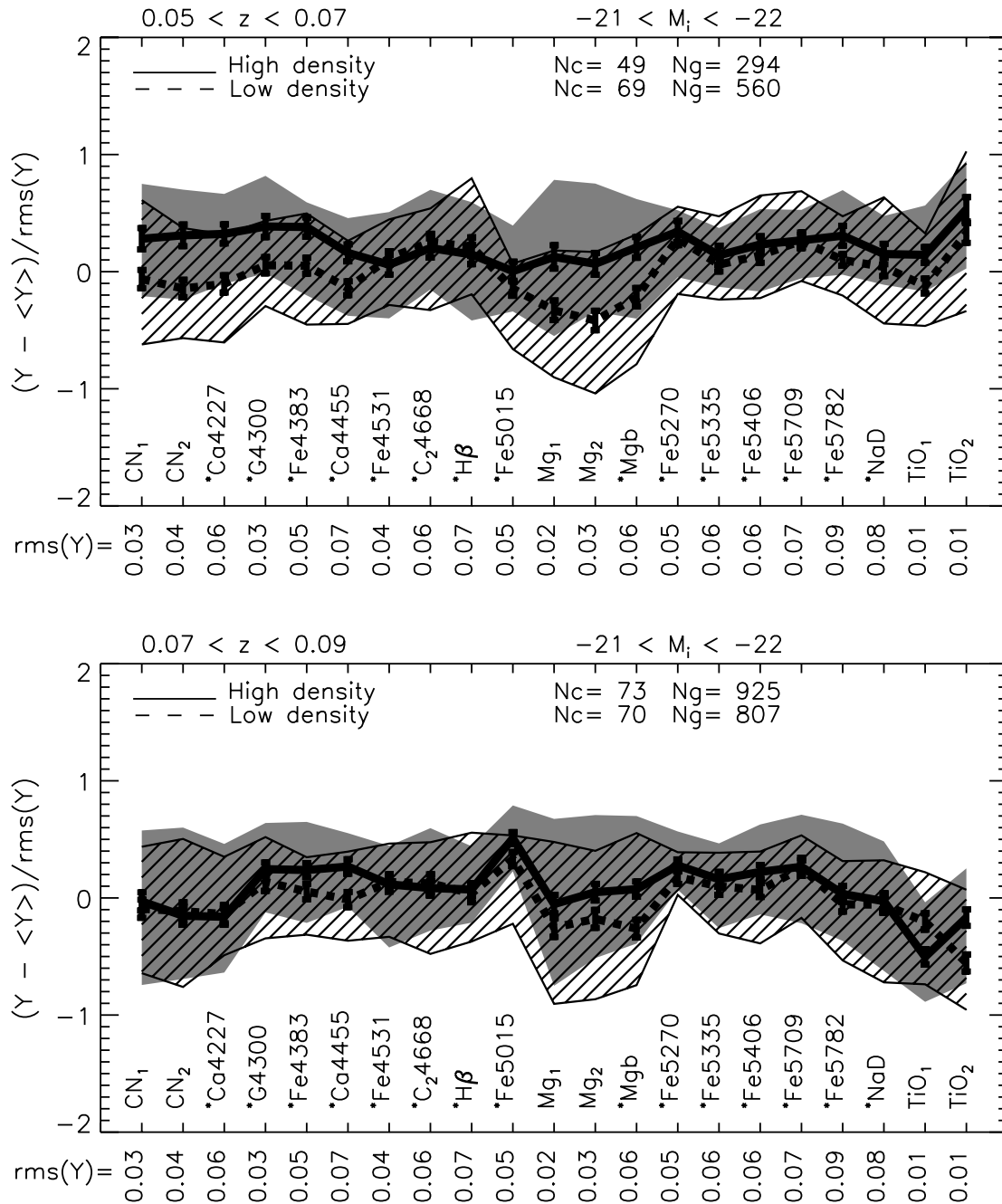


FIG. 7.—Lick indices for objects with the same narrow range of redshifts and luminosities as in Fig. 6. (An asterisk signifies that the quoted rms is for the logarithm of the index.) Recall that the mean luminosity and velocity dispersions are the same in dense and less dense environments, so trends with environment are not caused by correlations with σ . The bottom panel contains a supercluster, so environmental effects may not be accurate.

in small bins in luminosity and redshift (as indicated). Before we discuss individual parameters and indices further, note how similar the solid curves are in each set of panels: environmental effects are approximately the same in all our redshift and luminosity bins (with the possible exception of the $z \sim 0.08$ bin that includes the supercluster). Table 6, which quantifies trends with redshift, also quantifies these environmental trends.

Some of the differences between indices arise because the different observables correlate differently with luminosity (e.g., mass correlates more strongly with luminosity than size or velocity dispersion, and they all correlate more strongly with luminosity than does color). If an observable correlates strongly

with luminosity, the rms spread reported along the bottom of each panel may be dominated by the rms spread in luminosities, rather than by the scatter at fixed luminosity (we discuss this again in § 5.3). The solid curves in the different panels show results for galaxies in a narrow bin in luminosity. In this case, even if age effects account for the full scatter in index strength at fixed luminosity, they will not account for the full rms spread (i.e., the one computed using the full range of luminosities).

Previous work indicates that the slope of the color-magnitude relation does not evolve out to redshifts of order unity, and this has been used to argue that residuals from the color-magnitude relation are indicators of age (e.g., Kodama et al. 1998; Blakeslee

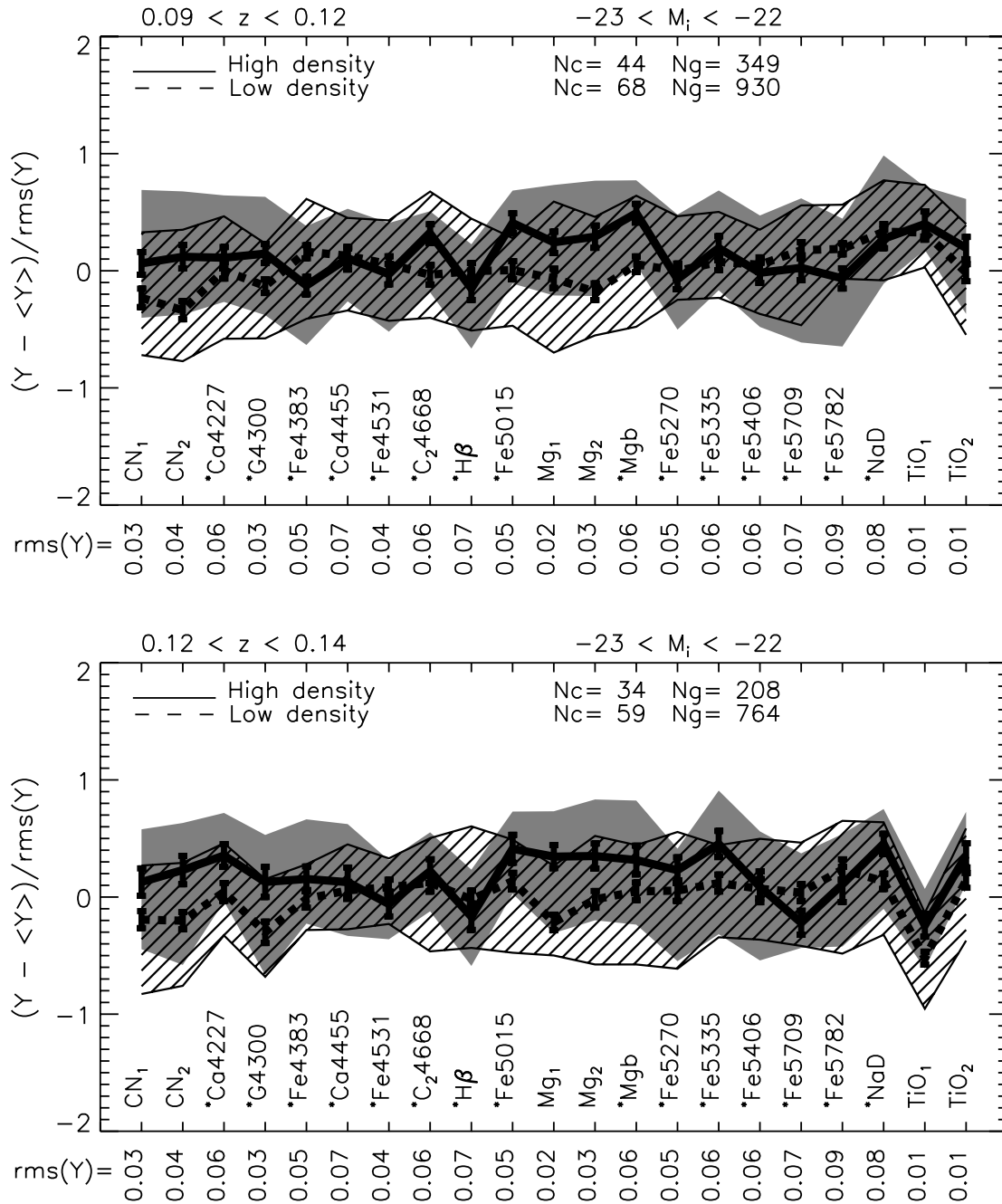


FIG. 7.—Continued

et al. 2003). Since the various panels in Figure 8 are for a small range in luminosity, in essence, the value of the dashed line for color shows the mean color residual from the color-magnitude relation. Hence, it is an age indicator. Since it shows the same variation as the solid line in the figure (the difference between cluster and lower density environments), the mean age difference between environments is approximately the same as the mean age difference between the two indicated redshifts: on average, objects in dense regions are less than ~ 1.3 Gyr older.

Like color, Mg shows approximately the same trends with environment as with redshift (Fig. 10), although the magnitude of both trends for Mg appears to be approximately half that for color. However, Mg correlates strongly with luminosity, and a substantial part of this apparent difference is because we are

only considering Mg for a small range in luminosity. If we account for this difference, then Mg and color are remarkably similar. If the age difference between cluster and low-density environments is ~ 1.3 Gyr, as suggested by color, then the similarity between the solid and dashed lines for Mg leaves little room for, e.g., metallicity effects. Section 5.3 provides a more quantitative model of these trends.

5.3. Interpretation: Evolution As a Clock

The typical age, metallicity, and α -abundance may change with environment. If trends with redshift primarily reflect age effects, then a comparison of the dashed and solid lines allows one to constrain the relative roles of age and metallicity and/or α -abundance on the different indices. A quantitative model is developed below.

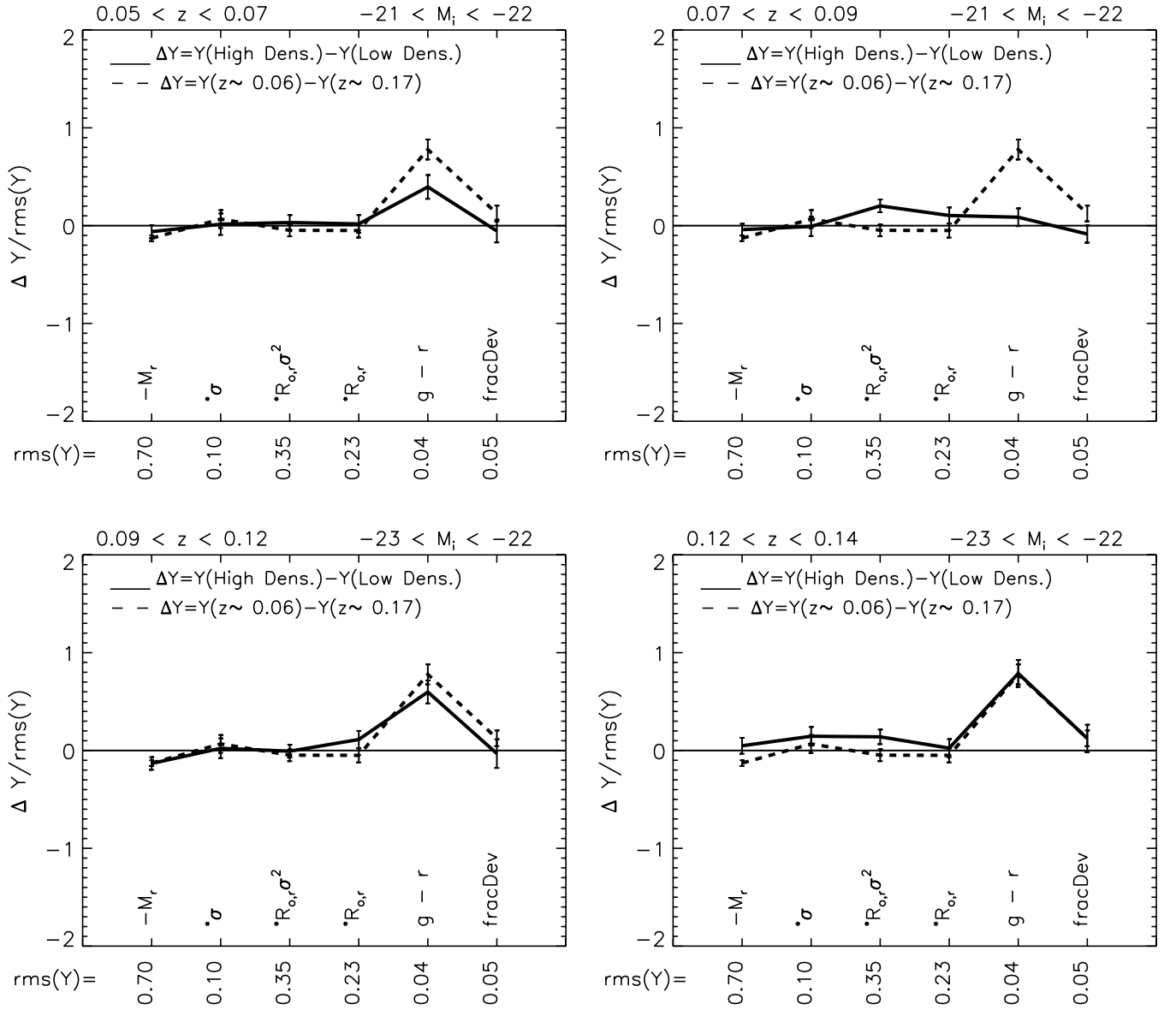


FIG. 8.—Evolution of observed parameters estimated using early-type galaxies in the entire sample that have $2.35 \leq \log \sigma \leq 2.4$ (dashed line in all panels), compared to dependence on environment (solid lines) for galaxies that have the range of redshift and luminosity shown in the top left and top right of each panel, respectively. The time difference between $z \sim 0.17$ and 0.06 is 1.3 Gyr. The top right panel is different from the others; it happens to contain a supercluster, and this may have compromised our estimates of environment or affected the color. (An asterisk signifies that the quoted rms is for the logarithm of the index.)

Suppose that the spread in index strength I is

$$\sigma_{II}^2(z) = [f_T^I(z)\sigma_T(z)]^2 + [f_X^I(z)\sigma_X(z)]^2, \quad (1)$$

where $T = \log(\text{age})$ and X represents other effects (e.g., it could be $\log(\text{metallicity})$), f_T^I describes how sensitive index I is to age, f_X^I describes how sensitive index I is to other effects (e.g., metallicity), and σ_T and σ_X denote the spread in ages and the spread in everything else. Note that it is the combination $f_T\sigma_T$ rather than the two terms individually that determines the contribution of age effects to the spread in index values. Also note that σ_T and σ_X are the same for all indices. (The expression above really follows from assuming that index strengths are determined by some, possibly degenerate, combination of age and other effects. For instance, if X is mainly sensitive to metallicity, then the expression above is a consequence of the

age-metallicity degeneracy. Models suggest that, in this case, $f_X/f_T = 3/2$.)

If the only difference between the population at two redshifts is age, then the change in index strength is

$$\Delta I_{\text{evol}} = f_T^I \Delta T_{\text{evol}}, \quad (2)$$

where ΔT denotes the change in T between the two epochs. (This actually assumes that f_T^I is the same for the two epochs and that the other effects such as metallicity are also. This is unlikely to be correct if the age difference between the two epochs is large, so this really assumes that the two epochs are close in units of the timescale over which the relations between index strength and age and metallicity change.) This provides an estimate for f_T^I in terms of observables.

Consider what this implies for color. It is often argued that residuals from the color-magnitude relation are indicators of age.

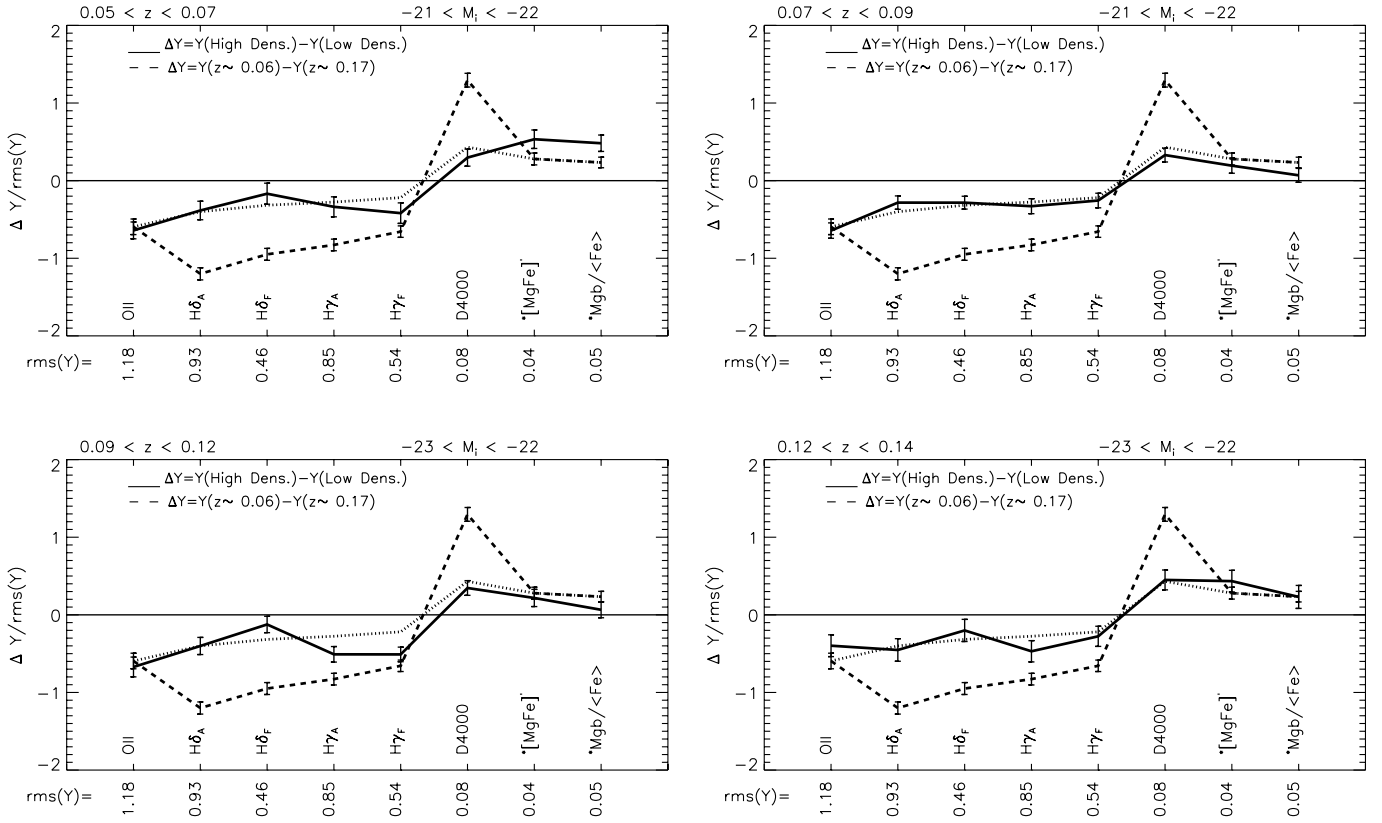


FIG. 9.—Evolution of the observed parameter (*dashed/dotted lines in all panels*) compared to dependence on environment (*solid lines*). Dotted lines correct for flux calibration problems by dividing measured values by a factor of 3 (see Appendix B). (An asterisk signifies that the quoted rms is for the logarithm of the index.) In most cases, the difference between $z \sim 0.17$ and 0.06 is similar to the difference between cluster and less dense environments.

In such a model, the full spread in colors comes from the scatter in color at fixed magnitude, plus a term that accounts for additional effects:

$$\sigma_{CC}^2 = \sigma_{C|M}^2 + (f_X^C \sigma_X)^2. \quad (3)$$

Therefore,

$$\begin{aligned} f_T^C \sigma_T &= \sigma_{C|M} \equiv \sigma_{CC} \sqrt{1 - \xi_{CM}^2}, \\ f_X^C \sigma_X &= \sqrt{\sigma_{CC}^2 - \sigma_{C|M}^2} \equiv \sigma_{CC} \xi_{CM}. \end{aligned} \quad (4)$$

(Section 5.2 included a discussion of the relative roles of the scatter at fixed luminosity and the slope of the index-luminosity relation. In the present context of the scatter in color, these are $\sigma_{C|M}$ and $\xi_{CM} \sigma_{CC}$: the scatter in colors at fixed magnitudes dominates if $|\xi_{CM}| \ll 1$.)

Since $\Delta C = f_T^C \Delta T$, σ_T equals that ΔT for which $\Delta C = \sigma_{C|M}$. To illustrate, in the SDSS data set studied in the main text, $\Delta C_{\text{evol}} = 0.031$ when ΔT_{evol} corresponds to a time interval of 1.3 Gyr. Therefore, the time interval required to produce a color change of $\sigma_{C|M}$ is

$$\sigma_T = (\Delta T_{\text{evol}} / \Delta C_{\text{evol}}) \sigma_{C|M}. \quad (5)$$

Since $\sigma_{C|M}$ is also measurable (the data indicate $\sigma_{C|M} = 0.037$), one has calibrated the relation between age and color.

Now consider other indices. We observe a change $\Delta I_{\text{evol}} = f_T^I \Delta T_{\text{evol}}$, so, over the range σ_T , the change in index strength would have been

$$\begin{aligned} f_T^I \sigma_T &= f_T^I \Delta T_{\text{evol}} (\sigma_T / \Delta T_{\text{evol}}) = \Delta I_{\text{evol}} (\sigma_T / \Delta T_{\text{evol}}) \\ &= \Delta I_{\text{evol}} (\sigma_{C|M} / \Delta C_{\text{evol}}). \end{aligned} \quad (6)$$

All the terms on the right-hand side are observables, so $f_T^I \sigma_T$ can be estimated from the data. Since $f_T^I \sigma_T$ is the first term on the right-hand side of equation (1), and the left-hand side of equation (1) is also measured,

$$f_X^I \sigma_X = \sqrt{\sigma_{II}^2 - \Delta I_{\text{evol}}^2 (\sigma_{C|M} / \Delta C_{\text{evol}})^2} \quad (7)$$

can also be estimated from the data.

The relative importance of age to other effects on the distribution of index strengths is given by the ratio

$$\begin{aligned} \frac{f_X^I \sigma_X}{f_T^I \sigma_T} &= \sqrt{\left(\frac{\sigma_{II}}{\Delta I_{\text{evol}}} \frac{\Delta T_{\text{evol}}}{\sigma_T} \right)^2 - 1} \\ &= \sqrt{\left(1.74 \frac{0.33 \sigma_{II}}{\Delta I_{\text{evol}}} \frac{\Delta C_{\text{evol}} / \sigma_{C|M}}{0.031 / 0.037} \right)^2 - 1}, \end{aligned} \quad (8)$$

where the first line follows from equations (1) and (2) and the second line uses the fact that $\sigma_{C|M} / \Delta C_{\text{evol}} = \sigma_T / \Delta T_{\text{evol}}$

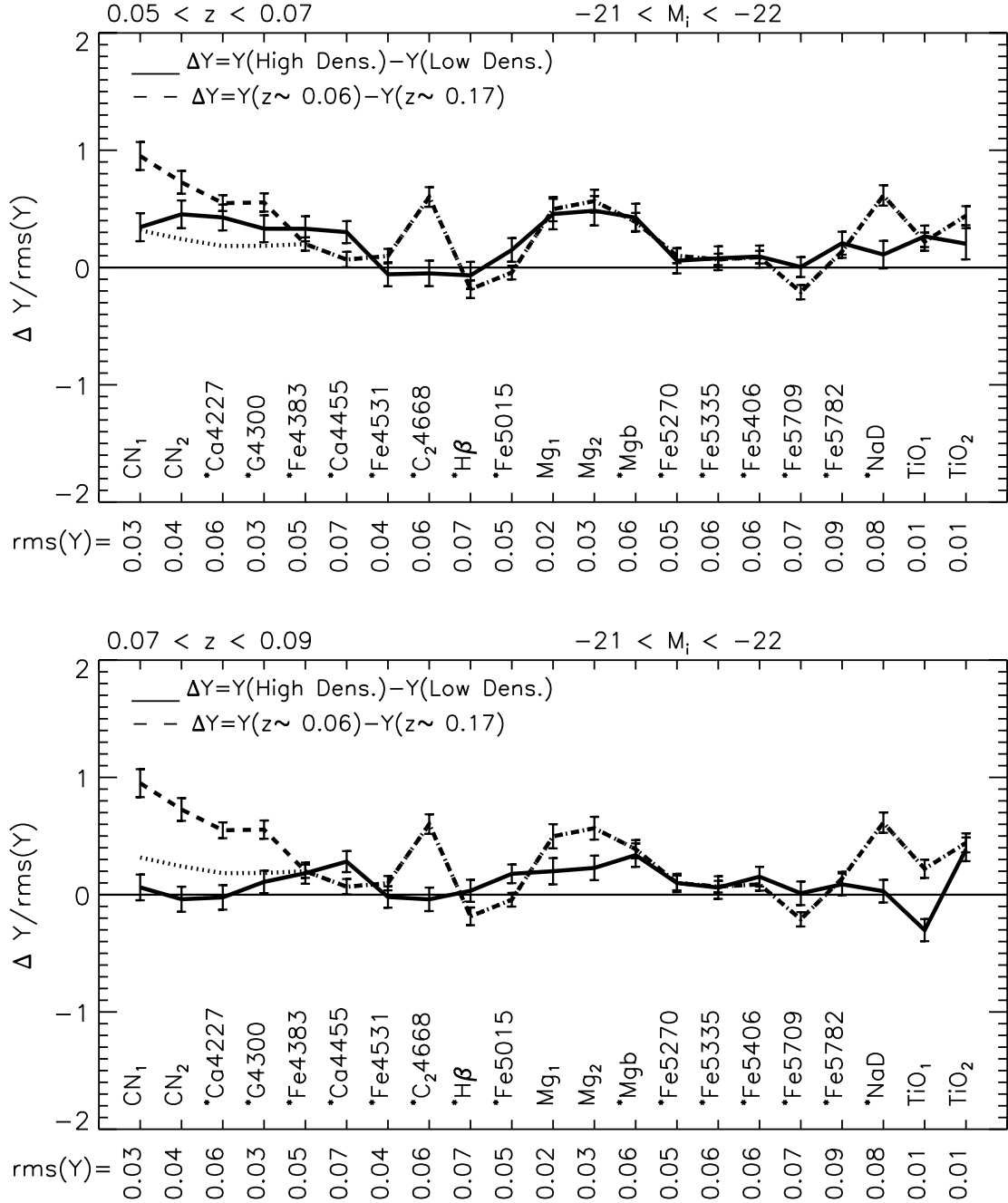


FIG. 10.—As for Fig. 9, but comparing the evolution of the Lick indices with the dependence on environment. The bottom panel contains a supercluster, so environmental effects may not be accurate. (An asterisk signifies that the quoted rms is for the logarithm of the index.)

(eq. [5]), and writes everything in units of typical observed values (e.g., Mg, [MgFe]['], and D4000 all have $\Delta I_{\text{evol}}/\sigma_{II} \approx 0.4$). Since $\Delta T_{\text{evol}}/\sigma_T$ is the same for all indices, larger values of $\Delta I_{\text{evol}}/\sigma_{II}$ indicate that a larger fraction of the spread in index strengths comes from age-related effects. Thus, age determines a larger fraction of the observed spread in colors than it does for Mg, and ages matter even less for the spread in Fe values.

In addition to comparing the relative roles of age and other effects for a given index, we can also compare indices with one another. For instance, although σ_X is not known, we know that it is the same for all indices I . Therefore, if we measure $\sigma_{CC}^2 - \Delta I_{\text{evol}}^2 (\sigma_{C|M}/\Delta C_{\text{evol}})^2$ for two indices and compute the ratio, then the result equals the ratio of $(f_X^I)^2$ for the two indices. This

allows a calibration of the relative sensitivities of the two indices to effects included in X . Thus,

$$\frac{f_X^{\text{Mgb}}}{f_X^C} = \sqrt{\frac{0.06^2 - (0.020\sigma_{C|M}/0.031)^2}{\sigma_{CC}^2 - \sigma_{C|M}^2}} = 3.44, \quad (9)$$

whereas

$$\frac{f_X^{\text{Mgb}}}{f_X^{\text{Fe}}} = \sqrt{\frac{0.06^2 - (0.020/0.031)^2 \sigma_{C|M}^2}{0.05^2 - (0.005/0.031)^2 \sigma_{C|M}^2}} = 1.11. \quad (10)$$

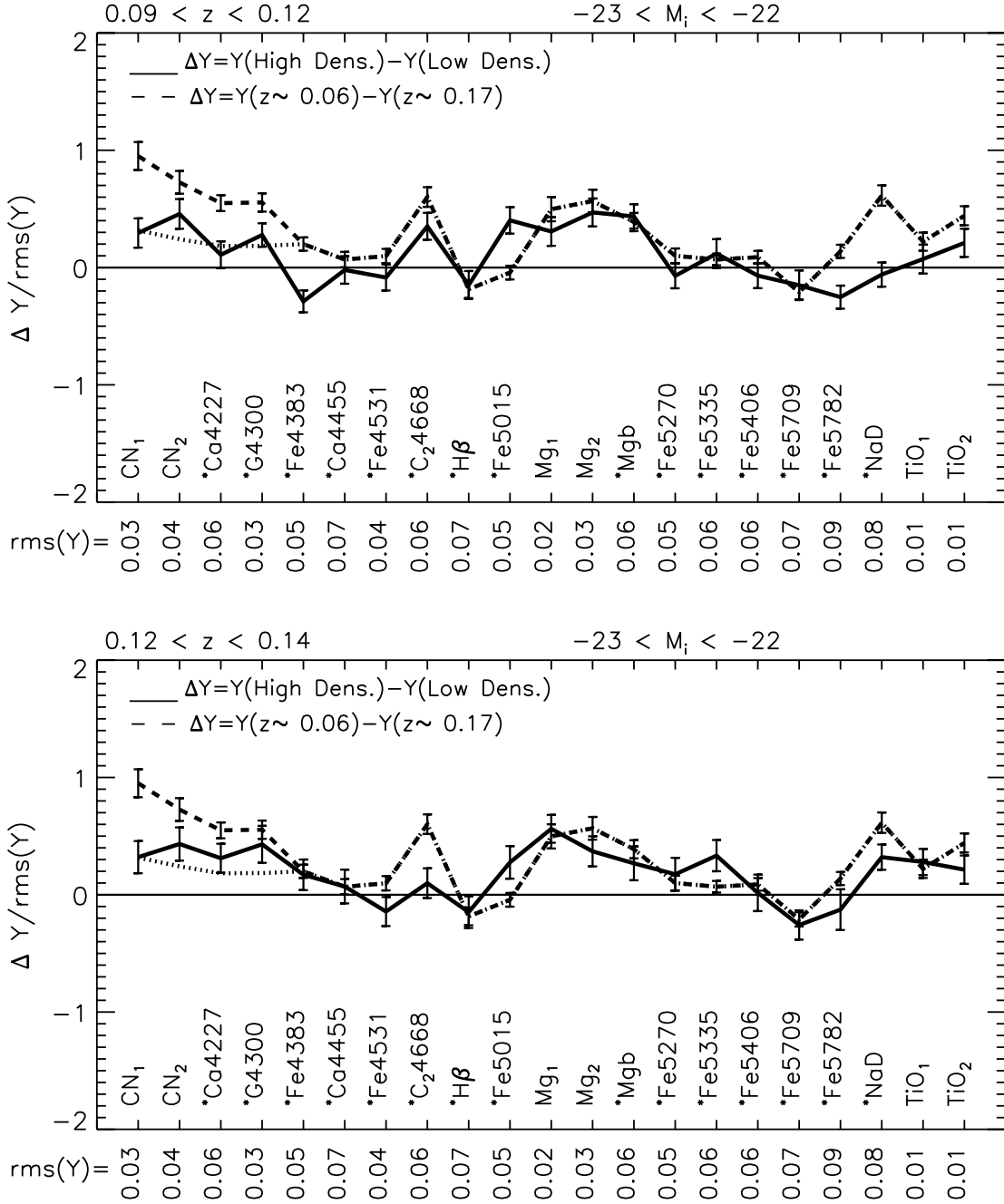


FIG. 10.—Continued

This indicates that color is less sensitive to effects such as metallicity than are Mg or Fe (or, e.g., metallicity and α -enhancement effects on color cancel each other, whereas they do not cancel as strongly for Mg and Fe).

We can proceed further if we are willing to make more model-dependent assumptions. In models in which residuals from the color-magnitude relation are age indicators, it is usually assumed that metallicity $\propto L^\beta$. Therefore, $\sigma_Z = 0.4\beta\sigma_{MM}$, where σ_{MM} denotes the rms spread in magnitudes.

If X is mainly sensitive to metallicity, then

$$f_X^I = \frac{2.5}{\beta} \frac{\sigma_{CC}}{\sigma_{MM}} \sqrt{\left(\frac{\sigma_{II}}{\Delta I_{evol}} \frac{\Delta C_{evol}}{\sigma_{CC}}\right)^2 - 1 + \xi_{C|M}^2}. \quad (11)$$

If we set $\sigma_{CC} = 0.04$, $\sigma_{MM} = 0.71$, $\xi_{C|M} = 0.4$, $\Delta C_{evol} = 0.031$, and $\Delta I_{evol}/\sigma_{II} \approx 0.33$ (as it is for Mg, $[MgFe]'$, and D4000), then

$$\frac{f_X^I}{f_T^I} = \frac{2.5}{\beta} \frac{0.04}{0.71} \frac{2.16}{f_T^I} = \frac{0.30}{\beta} \frac{\Delta T_{evol}}{\Delta C_{evol}} = \frac{0.44}{\beta}. \quad (12)$$

To obtain $f_X = (3/2)f_T$ as models suggest would require $\beta = 0.3$: this is not inconsistent with single-burst models (e.g., Bruzual & Charlot 2003) of the color-magnitude relation (Bernardi et al. 2005). The implied spread in metallicity across the population is $\sigma_Z = 0.4\beta\sigma_{MM} = 0.08$.

The behavior of Fe is difficult to explain in such a model. Figure 10 indicates that the trends with redshift and environment

are weak. The lack of evolution is suggestive of Fe being sensitive to effects other than age. But if there is a metallicity-luminosity correlation, as suggested above, one would expect to see an Fe-luminosity correlation. There is no such correlation in our data set (e.g., see Fig. 18).

5.4. Comparison of Evolution and Environment

Section 5.3 studied the effects of fixing the metallicity and varying the redshift by a small amount. Here, we fix the redshift and vary the environment. In this case,

$$\Delta I_{\text{env}} = f_T^I \sigma_T \frac{\Delta T_{\text{env}}}{\sigma_T} + f_X^I \sigma_X \frac{\Delta X_{\text{env}}}{\sigma_X}. \quad (13)$$

This illustrates that age differences can be compensated for by associated changes in X .

Many of the indices have $\Delta I_{\text{env}} = \Delta I_{\text{evol}}$. In this case

$$f_T^I \Delta T_{\text{evol}} = f_T^I \sigma_T \frac{\Delta T_{\text{env}}}{\sigma_T} + f_X^I \sigma_X \frac{\Delta X_{\text{env}}}{\sigma_X}, \quad (14)$$

so

$$\frac{\Delta T_{\text{env}}}{\sigma_T} = \frac{\Delta T_{\text{evol}}}{\sigma_T} - \frac{f_X^I \sigma_X}{f_T^I \sigma_T} \frac{\Delta X_{\text{env}}}{\sigma_X}. \quad (15)$$

If $\Delta X_{\text{env}} = 0$, then the mean age difference between environments is the same as the mean age difference between two epochs, but in general, a larger or smaller age difference can be compensated for by an associated change in X , and $(f_X \sigma_X / f_T \sigma_T)$ governs how large this change must be.

For the indices where $\Delta I_{\text{env}} \approx \Delta I_{\text{evol}} \approx 0.33 \sigma_I$ (e.g., Mg),

$$\frac{\Delta T_{\text{env}}}{\sigma_T} = \frac{\Delta T_{\text{evol}}}{\sigma_T} - 1.42 \frac{\Delta X_{\text{env}}}{\sigma_X} = 0.84 - 1.42 \frac{\Delta X_{\text{env}}}{\sigma_X};$$

evidently, objects in the densest regions of our sample are older than those in the least dense regions, unless they have larger X -values (e.g., they are more metal-rich) by $(0.84/1.42)\sigma_X$. Alternatively, if the objects in dense regions have smaller X -values (e.g., they are metal-poor), then the age difference between environments can be larger than 0.84 times the rms age variation across the sample.

The age- X degeneracy can be broken if we again consider color. Our estimate of environmental effects uses a small range of magnitudes in any given redshift bin, so, in effect, we are studying residuals from the color-magnitude relation in different environments. If these residuals are only sensitive to age, they have $f_X^{C|M} = 0$. Therefore,

$$\Delta T_{\text{env}} = \Delta C_{\text{env}} / f_T^{C|M} = \Delta C_{\text{env}} / (\Delta C_{\text{evol}} / \Delta T_{\text{evol}}).$$

It happens that $\Delta C_{\text{env}} \approx \Delta C_{\text{evol}}$, so $\Delta T_{\text{env}} \approx \Delta T_{\text{evol}}$. This age difference must be independent of the index that was used to estimate it. Now consider other indices for which $\Delta I_{\text{env}} \approx \Delta I_{\text{evol}}$ (e.g., Mg, Fe, and D4000). Since equation (15) describes these indices, and $f_X \sigma_X / f_T \sigma_T$ is of order unity (eq. [8]), it must be that $\Delta X_{\text{env}} / \sigma_X \ll 1$.

The fact that Mg behaves similarly to color suggests that the entire environmental variation of Mg can be accounted for by age effects: metallicity effects are not very important. This leads to a provocative conclusion: claims that metallicity effects are important for explaining the weak environmental dependence of Lick index strengths such as Mg are incompatible with currently popular interpretations of the color-magnitude relation.

6. COMPARISON WITH STELLAR POPULATION SYNTHESIS MODELS

Section 5 argued that our data are consistent with the hypotheses that the stellar populations of early-type galaxies in dense regions are slightly older than in less dense regions, and that metallicity differences between environments are negligible. This section shows that using single-burst stellar population synthesis models to interpret our data results in qualitatively similar conclusions.

6.1. The Models

The models are characterized by three numbers: age, metallicity, and α -enhancement. In most of the plots that follow, these models are evaluated on a grid of age 2, 3, 5, 10, and 15 Gyr, metallicity $[Z/H] = -0.33, 0, 0.35$, and 0.67 , and $[\alpha/\text{Fe}] = 0, 0.3$, and 0.5 , and we interpolate linearly between these grid points.

The effects of nonsolar $[\alpha/\text{Fe}]$ values have been considered by Tripicco & Bell (1995) and incorporated into models by Trager et al. (2000), TMB03, TMK04, and Tantalo & Chiosi (2004). In what follows we have chosen to concentrate on the models of TMB03 and TMK04. However, the interpretations that follow are necessarily model dependent, and we caution that different models sometimes differ substantially from one another, so the resulting interpretations should be treated with caution. Indeed, Tantalo & Chiosi (2004) show that their α -enhanced models can differ substantially from those of other groups and have argued that uncertainties in how one treats $[\text{Ti}/\text{Fe}]$ can have important effects. Hence, they argue strongly that the tendency to draw strong conclusions from such models is unwarranted.

To illustrate the point that all quantitative conclusions that follow are model dependent, Figure 11 compares the evolution of $H\beta$, $H\gamma_F$, Mg b , and Fe in the models of TMB03 and TMK04 with the models of Bruzual & Charlot (2003). The model tracks are for solar $[\alpha/\text{Fe}]$, because the Bruzual-Charlot models do not yet include nonsolar $[\alpha/\text{Fe}]$. The solid and dashed curves in each panel show the Bruzual-Charlot models for two values of the metallicity (solar and greater than solar). The three dotted curves in each panel show the TMB03 and TMK04 models for three different metallicities (solar and above, all at solar α -enhancement). In all panels, the models agree at solar metallicity (the solid curve is close to the dotted one). However, in some panels the Bruzual-Charlot models are more like the highest metallicity TMB03 and TMK04 models (e.g., $H\beta$), whereas in others, they are more like the intermediate-metallicity models (e.g., $H\gamma_F$).

To see that these differences matter, consider the two curves close to the center in the top right panel. Although the two models differ by 10% at fixed age, they differ by 100% at fixed $\langle \text{Fe} \rangle$. Since it is $\langle \text{Fe} \rangle$ that is observed, any quantitative conclusions about metallicity and age are strongly model dependent.

The figure also shows that the differences between the ages inferred from the models depend on whether one uses $H\beta$ or the higher order Balmer lines $H\gamma_F$, and that these differences can be substantial. The plot above suggests that one would infer younger ages from $H\gamma_F$ than from $H\beta$, a point we return to below.

6.2. The Method

Figure 12 shows the distribution of $H\beta$ versus Mg (*left*), $\langle \text{Fe} \rangle$ versus Mg (*middle*), and $H\beta$ versus $\text{Mg}/\langle \text{Fe} \rangle$ (*right*). Table 7 gives these index strengths at Lick rather than SDSS resolution. [Recall that $\langle \text{Fe} \rangle = (\text{Fe}5270 + \text{Fe}5335)/2$.] In this and the figures that follow, we have divided the sample into the same small

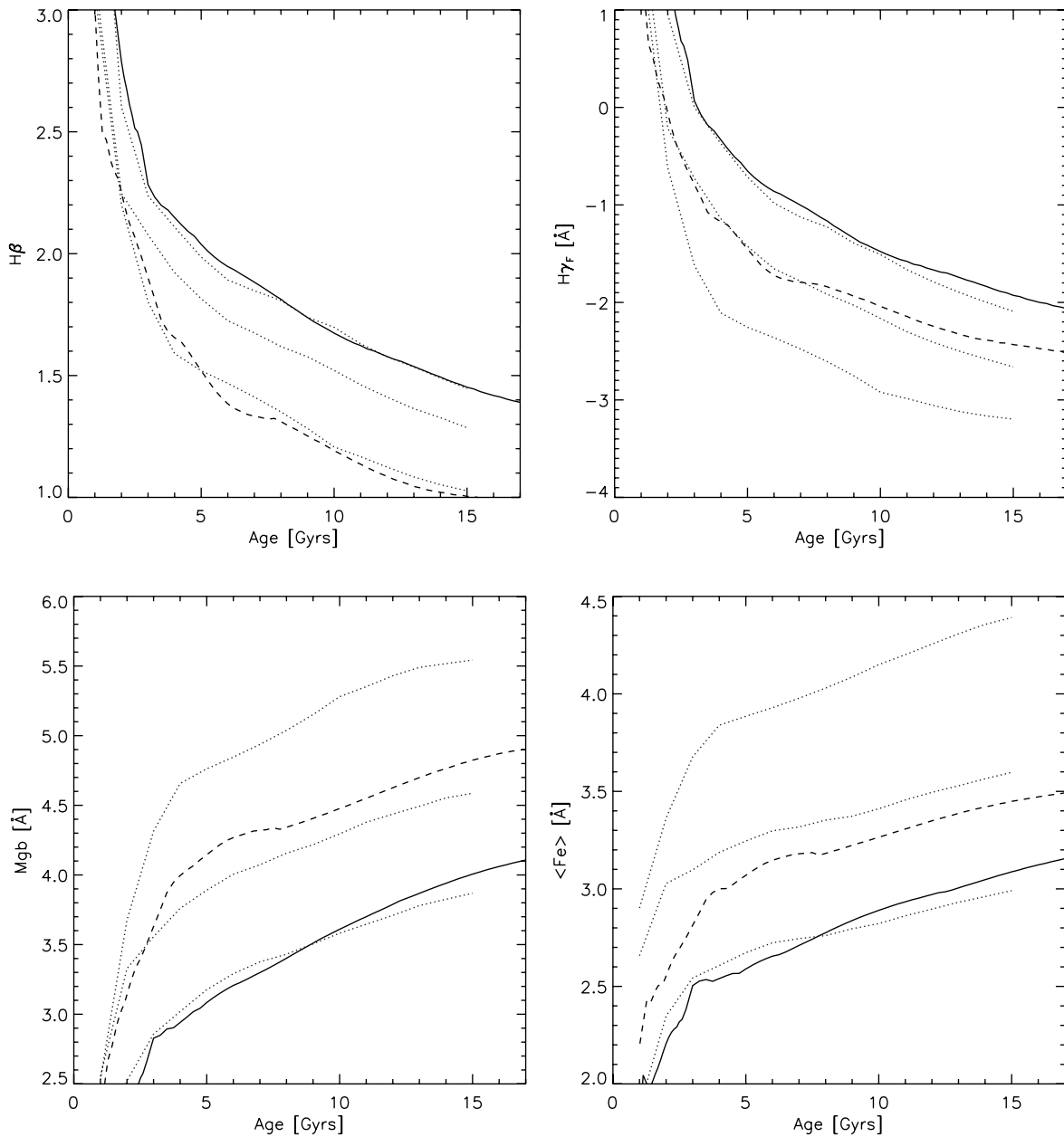


FIG. 11.—Evolution of various absorption-line strengths in single-burst stellar population synthesis models at solar α -enhancement. Solid and dashed lines show the models of Bruzual & Charlot (2003) at solar metallicity and higher. Dotted lines show the models of TMB03 and TMK04 at solar metallicity and higher. The models agree at solar metallicity (bottom curves in Mg b and $\langle\text{Fe}\rangle$, top curves in $H\beta$ and $H\gamma_F$) but, in general, do not agree at the higher metallicities expected to be characteristic of the early-type population. [See the electronic edition of the *Journal* for a color version of this figure.]

bins in redshift as in the previous figures so as to be able to separate out the effects of evolution. In addition, symbol sizes have been scaled to reflect the number of galaxies that made up the composites they represent.

The grids in each panel show the TMB03 models. The solid and dashed grids in the left panels show age and metallicity at α -enhancements of 0 (solar) and 0.3. This choice of observables separates out age and metallicity quite clearly. The observables in the middle panels separate out metallicity and α -enhancement nicely: solid and dashed grids show metallicity and α -enhancement for ages of 10 and 15 Gyr. The solid and dashed grids in the right panels show ages and α -enhancements when the metallicity is solar and 0.35, respectively.

We determine ages, metallicities, and α -enhancements for each data point from these grids as follows: We begin with a guess for the α -enhancement (e.g., solar). Then the $H\beta$ -Mg plot pro-

vides estimates of the age and metallicity (by linear interpolation in the model grid). We then use the $\langle\text{Fe}\rangle$ -Mg grid associated with the age estimate to estimate a metallicity and α -enhancement. If this new α -enhancement differs substantially from our initial guess, we return to the $H\beta$ -Mg plot but then use the new α -enhancement to reestimate the age and metallicity from the model, and use the new age estimate to determine the appropriate $\langle\text{Fe}\rangle$ -Mg model with which to estimate $[Z/H]$ and $[\alpha/\text{Fe}]$ for the data point. We continue iterating this procedure until consistent ages, metallicities, and α -enhancements have been obtained. Typically, this happens after about five iterations. These provide our first estimates of self-consistent values of age, $[Z/H]$, and $[\alpha/\text{Fe}]$.

We then repeat this process, but then using the $\langle\text{Fe}\rangle$ -Mg and $H\beta$ -Mg/ $\langle\text{Fe}\rangle$ plots. (That is, we begin with a guess for the age, determine the metallicity and α -enhancement from the

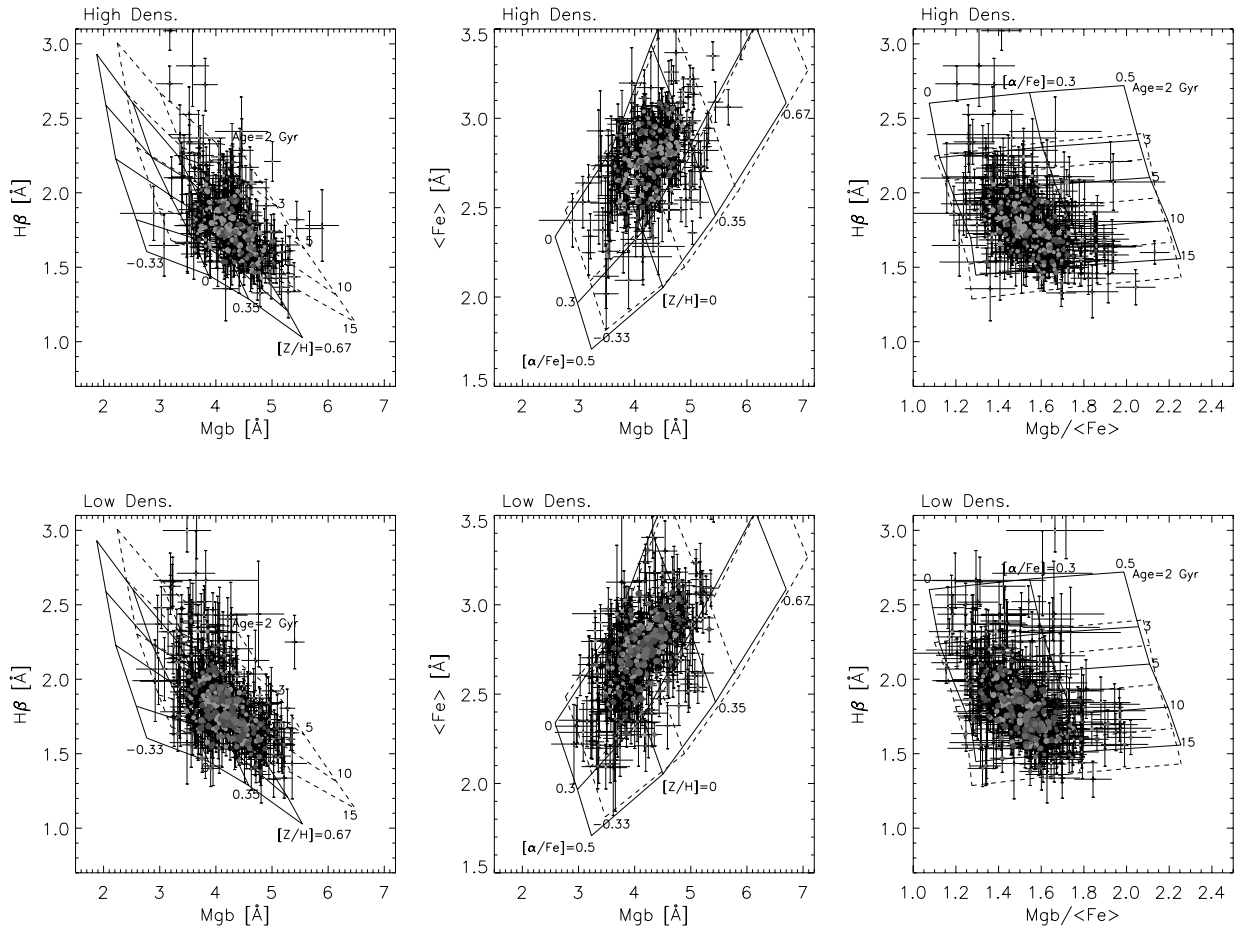


FIG. 12.—Distribution of $H\beta$ vs. Mg (left panels), $\langle Fe \rangle$ vs. Mg (middle panels), and $H\beta$ vs. $Mg/\langle Fe \rangle$ (right panels) for two different environments. Symbol sizes indicate the number of galaxies in the associated composite. Grids show the models of TMB03. Solid and dashed grids show age and metallicity at α -enhancements that are 0 (solar) and 0.3 (left panels), metallicity and α -enhancement for ages of 10 and 15 Gyr (middle panels), and ages and α -enhancements when $[Z/H]$ is 0 and 0.35 (right panels). [See the electronic edition of the Journal for a color version of this figure.]

model grid for $\langle Fe \rangle$ - Mg , and use this metallicity to determine the model grid to use for the $H\beta$ - $Mg/\langle Fe \rangle$ diagnostic. In turn, this provides revised estimates for the age and α -enhancement; the new age estimate is then used in the $\langle Fe \rangle$ - Mg diagram. This is repeated until a new self-consistent triple of age, $[Z/H]$, and $[\alpha/Fe]$ has been found.) Finally, we repeat all this using the $H\beta$ - $Mg/\langle Fe \rangle$ and $H\beta$ - Mg plots. Thus, we have three estimates of age, $[Z/H]$, and $[\alpha/Fe]$ that we can use to test for self-consistency (see § 6.3).

It is particularly important to estimate the typical uncertainty on the derived parameters that are due to the measurement errors because the model grids are not aligned with the axes of

observables in Figure 12, so these uncertainties will be correlated (e.g., Trager et al. 2000). We do this as follows: We compute the typical uncertainties in the measurements of $H\beta$, Mg , and $\langle Fe \rangle$ (the errors on $Mg/\langle Fe \rangle$ are easily derived from those on Mg and $\langle Fe \rangle$). We then generate 27 mock “galaxies” by adding and subtracting the reported measurement errors to the mean observed values of $H\beta$, Mg , and $\langle Fe \rangle$, and hence $Mg/\langle Fe \rangle$ (we use mean, mean plus error, and mean minus error for each of the three observables). We then run the algorithm described above for each of these model “galaxies.” This provides three estimates of age, $[Z/H]$, and $[\alpha/Fe]$ for each of the 27 objects. The resulting distribution of points in the age, $[Z/H]$, and $[\alpha/Fe]$

TABLE 7
LICK INDEX STRENGTHS AND UNCERTAINTIES USED TO MEASURE AGE, $[Z/H]$, AND $[\alpha/Fe]$ FROM SSP MODELS

ID	$H\gamma_F$ (Å)	Err (Å)	$H\beta$ (Å)	Err (Å)	$Mg\ b$ (Å)	Err (Å)	Fe5270 (Å)	Err (Å)	Fe5335 (Å)	Err (Å)
1.....	-0.650	0.232	1.887	0.164	3.524	0.187	3.086	0.363	2.018	0.195
2.....	-0.983	0.192	1.935	0.144	4.138	0.160	2.511	0.298	2.226	0.172
3.....	-1.664	0.239	1.346	0.191	4.436	0.211	2.843	0.309	1.883	0.211
4.....	-1.524	0.143	1.654	0.114	4.457	0.108	3.474	0.165	2.531	0.110
5.....	-2.248	0.170	1.643	0.109	4.370	0.129	2.966	0.173	2.839	0.121

NOTES.—These were measured from the composite spectra given in Table 1 after convolving to Lick resolution. Table 7 is published in its entirety in the electronic edition of the *Astronomical Journal*. A portion is shown here for guidance regarding its form and content.

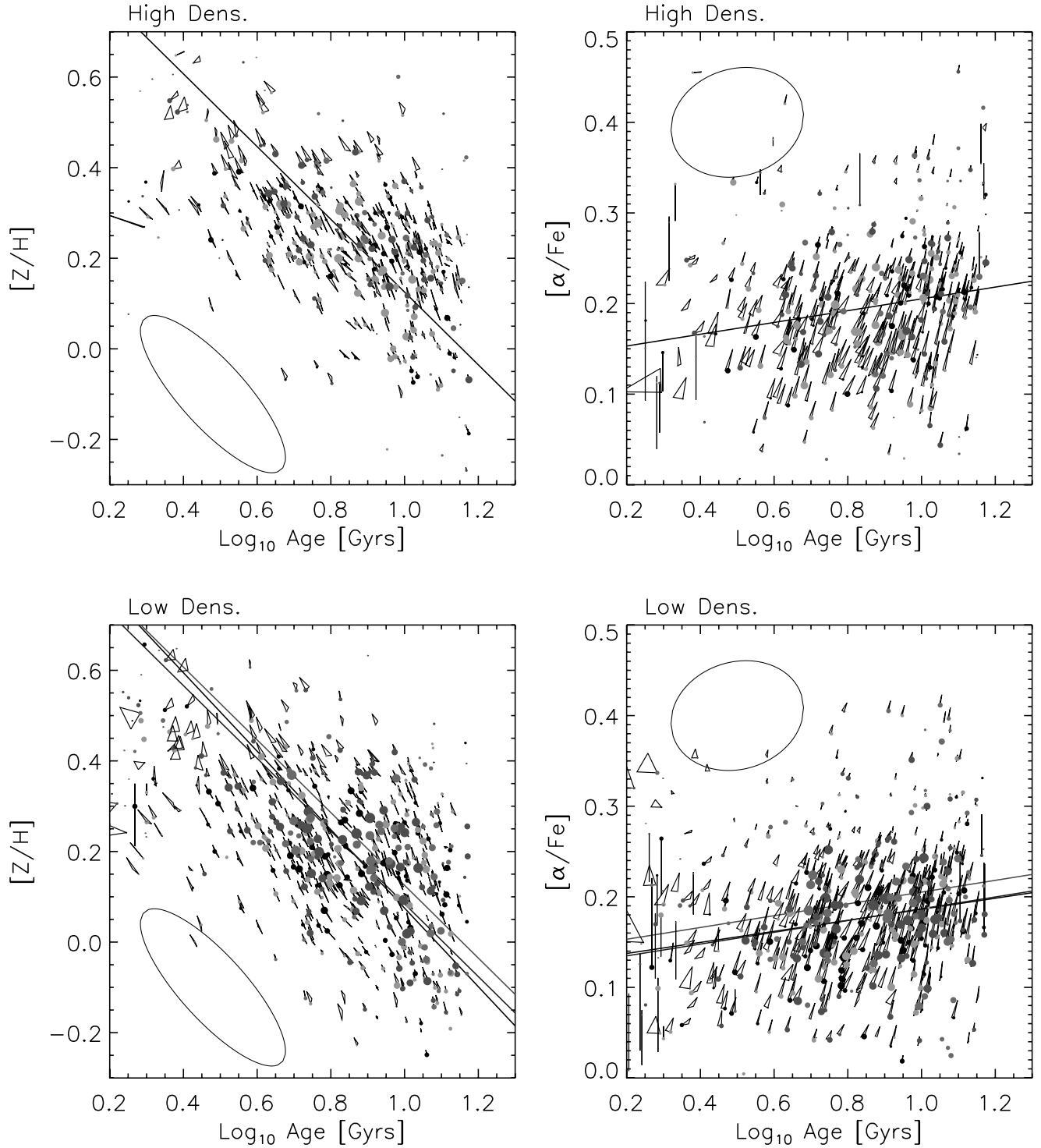


FIG. 13.—Pairwise correlations between derived ages, metallicities, and α -enhancements. The vertices of the triangle associated with each data point show the three estimates (see text) of each quantity; these provide a rough estimate of the systematic uncertainty in the derived quantities. The ellipse on the left of each plot shows the typical uncertainty arising from the errors associated with measuring the line indices. The shape of the ellipse in the left panels reflects the well-known degeneracy between age and metallicity. The solid lines in the top panels show bisector (*top left*) and direct (*top right*) fits. The solid lines in the bottom panels compare the offsets between high- and low-density environments if both samples are required to have the same slope as that shown in the top panel. [See the electronic edition of the *Journal for a color version of this figure*.]

TABLE 8

AGE, $[Z/H]$, AND $[\alpha/Fe]$ OBTAINED USING THE LICK INDEX STRENGTHS REPORTED IN TABLE 7 AND THE SSP MODELS OF TMB03 AND TMK04

ID	Age _{Hβ} (Gyr)	Err (Gyr)	$[Z/H]_{H\beta}$	Err	$[\alpha/Fe]_{H\beta}$	Err	Age _{Hγ_F} (Gyr)	Err (Gyr)	$[Z/H]_{H\gamma_F}$	Err	$[\alpha/Fe]_{H\gamma_F}$	Err
1.....	6.9	2.7	-0.017	0.089	0.102	0.065	4.8	2.4	0.059	0.082	0.123	0.044
2.....	5.9	2.1	0.105	0.082	0.326	0.059	7.6	3.4	0.062	0.076	0.313	0.042
3.....	0.0	0.0	0.000	0.000	0.000	0.000	0.0	0.0	0.000	0.000	0.000	0.000
4.....	8.7	3.3	0.302	0.131	0.144	0.042	6.4	2.4	0.359	0.051	0.162	0.036
5.....	9.6	3.4	0.225	0.107	0.150	0.069	0.0	0.0	0.000	0.000	0.000	0.000

NOTES.—Two sets of quantities are reported: the first set of columns were obtained using $H\beta$, $Mg\ b$ and $\langle Fe \rangle$, while the final six columns were obtained after substituting $H\gamma_F$ for $H\beta$. Objects with ages set to zero are those for which the models did not return reliable estimates of age, $[Z/H]$, and $[\alpha/Fe]$. This can be either because they lie beyond the model grids or because the three ways of estimating the ages give very different answers. Table 8 is published in its entirety in the electronic edition of the *Astronomical Journal*. A portion is shown here for guidance regarding its form and content.

plane forms our estimate of the full uncertainties in the derived parameters.

6.3. Results

From the three combinations of plots described in § 6.2, we have three different estimates of age, $[Z/H]$, and $[\alpha/Fe]$. If the procedure just described is self-consistent and the models are sufficiently realistic, one expects these three estimates to be similar. The extent to which this is the case is shown in Figure 13. Associated with each data point is a triangle, the vertices of which

represent the three estimates of the derived age, $[Z/H]$, and $[\alpha/Fe]$. The size of the triangle gives a rough estimate of the systematic uncertainty in the derived quantities associated with the model (i.e., assuming perfect measurements). The figure indicates that this uncertainty does not contribute significantly to the scatter in the various panels. Solid lines show the bisector fit to the relation in the top left panel and the direct fit to the relation in the right panels. These suggest that older systems tend to have smaller metallicities (*left panels*) and slightly larger α -enhancements (*right panels*).

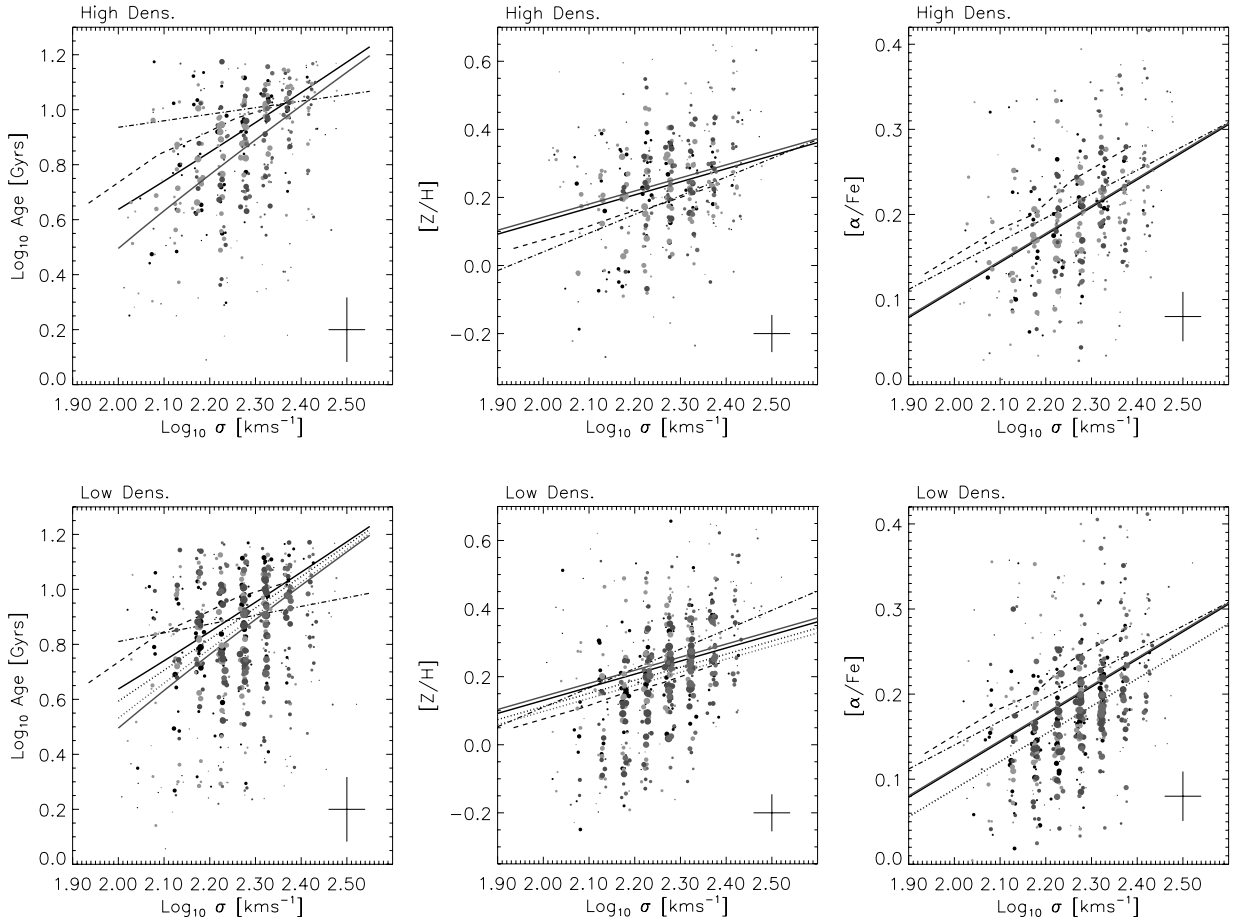


FIG. 14.—Objects with a large σ tend to be older (*left panels*) and have larger metallicities (*middle panels*) and larger α -enhancements (*right panels*). This is true at all redshifts in our sample: black lines show the mean relation at $z \sim 0.06$, and light lines show the result of fitting for the shift in gigayears for the sample at $z \sim 0.11$. Moreover, note that there is clear evolution in the age- σ relation but not in $[Z/H]$ - σ or $[\alpha/Fe]$ - σ . In addition, at fixed σ objects in dense regions (*solid lines*) tend to have similar ages and metallicities as their counterparts in less dense regions (*bottom panels, dotted lines*) and slightly larger α -enhancements. The cross in the bottom right corner of each panel shows the typical uncertainty. Dashed and dot-dashed lines show the relations obtained by Nelan et al. (2005) and Thomas et al. (2005) in their analysis of other data sets. [See the electronic edition of the *Journal* for a color version of this figure.]

TABLE 9
CORRELATIONS OF DERIVED PARAMETERS, AGE, $[Z/H]$, AND $[\alpha/Fe]$ WITH VELOCITY DISPERSION

Model	$\log(\text{age})-\log \sigma$	$[Z/H]-\log \sigma$	$[\alpha/Fe]-\log \sigma$
Using $H\beta$			
Slope	1.15	0.38	0.32
ZP	-1.72 ± 0.31	-0.64 ± 0.013	-0.54 ± 0.005
$\Delta ZP_{\text{evol}}(z \sim 0.06 \text{ to } \sim 0.08)$	0.27 ± 0.17 (Gyr)	0.008 ± 0.009	0.001 ± 0.004
$\Delta ZP_{\text{evol}}(z \sim 0.06 \text{ to } \sim 0.11)$	1.21 ± 0.31 (Gyr)	-0.011 ± 0.013	-0.002 ± 0.006
$\Delta ZP_{\text{evol}}(z \sim 0.06 \text{ to } \sim 0.13)$	0.81 ± 0.47 (Gyr)	0.008 ± 0.019	0.005 ± 0.010
$\Delta ZP_{\text{env}}(z \sim 0.06)$	0.42 ± 0.38 (Gyr)	0.018 ± 0.016	0.023 ± 0.006
$\Delta ZP_{\text{env}}(z \sim 0.08)$	0.41 ± 0.28 (Gyr)	0.016 ± 0.014	0.017 ± 0.005
$\Delta ZP_{\text{env}}(z \sim 0.11)$	-0.27 ± 0.37 (Gyr)	0.044 ± 0.016	0.025 ± 0.007
$\Delta ZP_{\text{env}}(z \sim 0.13)$	0.63 ± 0.55 (Gyr)	0.025 ± 0.022	0.017 ± 0.011
Using $H\gamma_F$			
Slope	0.81	0.58	0.39
ZP	-0.98 ± 0.23	-1.07 ± 0.010	-0.68 ± 0.005
$\Delta ZP_{\text{evol}}(z \sim 0.06 \text{ to } \sim 0.08)$	0.17 ± 0.14 (Gyr)	0.006 ± 0.007	0.002 ± 0.003
$\Delta ZP_{\text{evol}}(z \sim 0.06 \text{ to } \sim 0.11)$	0.95 ± 0.20 (Gyr)	-0.003 ± 0.011	0.005 ± 0.006
$\Delta ZP_{\text{evol}}(z \sim 0.06 \text{ to } \sim 0.13)$	1.17 ± 0.41 (Gyr)	0.001 ± 0.017	0.006 ± 0.010
$\Delta ZP_{\text{env}}(z \sim 0.06)$	0.58 ± 0.28 (Gyr)	0.008 ± 0.013	0.022 ± 0.006
$\Delta ZP_{\text{env}}(z \sim 0.08)$	0.47 ± 0.21 (Gyr)	0.016 ± 0.011	0.017 ± 0.005
$\Delta ZP_{\text{env}}(z \sim 0.11)$	0.60 ± 0.24 (Gyr)	0.015 ± 0.013	0.014 ± 0.007
$\Delta ZP_{\text{env}}(z \sim 0.13)$	0.95 ± 0.46 (Gyr)	0.010 ± 0.020	0.014 ± 0.011

NOTES.—The first two rows show the fits (slope and zero point) to the high-density sample at $z = 0.06$. The following three rows show the offsets with respect to these fits for these relations at different redshifts. The last four rows show the offsets between different environments at different redshifts; the slope of the fit was kept fixed to the value given by the high-density sample at $z = 0.06$.

The ellipses in the left corner of each panel show the typical uncertainty on the derived parameters that come from the measurement errors; these dwarf the systematic uncertainties associated with our algorithm. In the left panels especially, the errors are strongly correlated, so that much of the apparent anticorrelation between age and metallicity is due to the errors. This anticorrelation of the errors tracks the well-known age-metallicity degeneracy associated with such models. Table 8 provides the derived ages, $[Z/H]$, and $[\alpha/Fe]$ values, with the associated error estimates, for each composite spectrum.

In all panels of Figure 13 the distribution of derived parameters is slightly, but not substantially, broadened by the errors. In particular, although the long axis of the distribution shown in the left panels has been broadened by the correlated errors, the shape of the error ellipse shows that the distribution along the shorter axis cannot have been significantly broadened. Trager et al. (2000) argued that the scatter in this direction is primarily due to scatter in σ : objects with the same σ lie parallel to this relation, with larger σ objects lying at larger ages and metallicities. A similar statement applies if we substitute $[\alpha/Fe]$ for σ . This is true of our data set also: at fixed σ (or $[\alpha/Fe]$), older objects appear to be metal-poor.

The panels on the bottom allow a comparison between environments. The lines show fits from the panels on the top, fits for a shift in the zero point while requiring the same slope, and fits for a shift in the zero point allowing the slope to vary. These fits indicate that there is a small offset between the age-metallicity correlation in the two environments and that objects in dense regions tend to have slightly larger α -enhancements than their counterparts of the same age in less dense regions.

Figure 14 shows all three derived quantities as a function of velocity dispersion in the two environments. (Because our three

estimates of the derived quantities tend to be so similar, we have not shown the triangles associated with each point. Also, note the selection effect; the high-redshift bins do not have objects at small σ .) In each panel, black solid lines show direct fits to the relations in the high-density regions at $z \sim 0.06$; light solid lines show the offset in gigayears, $[Z/H]$, and $[\alpha/Fe]$ required to fit the relations at $z \sim 0.11$. Dotted lines in the panels on the bottom show the result of fitting for the offsets (in gigayears, $[Z/H]$, and $[\alpha/Fe]$) from the solid curves that best fit the relations for the low-density sample. These fits show that, at any given redshift and in any environment, objects with large σ tend to be older (*left panels*) and have larger metallicities (*middle panels*) and larger α -enhancements (*right panels*). These fits are given in Table 9, which also quantifies trends with redshift and environment.

Comparison of the light and black curves shows that the high- and low-density samples are both qualitatively consistent with the hypothesis of passively evolving populations: at fixed σ , the high-redshift objects are younger, but there is no evolution in $[Z/H]$ and $[\alpha/Fe]$. Moreover, the age difference is consistent with the redshift difference in our assumed cosmology.

Comparison of the solid and dotted lines in the panels on the bottom allows a study of the effects of environment. These indicate that at fixed σ , objects in dense regions tend to have the same ages and metallicities as their counterparts in less dense regions, but they have slightly larger α -enhancements. In contrast, Thomas et al. (2005) found that objects in less dense regions are slightly younger and more metal-rich, but they find no α -enhancement effect (see also Kuntschner et al. 2001).

To study this further, dot-dashed lines show the fits reported by Thomas et al. (2005). Whereas our metallicity- σ and $[\alpha/Fe]$ - σ values tend to be slightly different from theirs, our age- σ relations

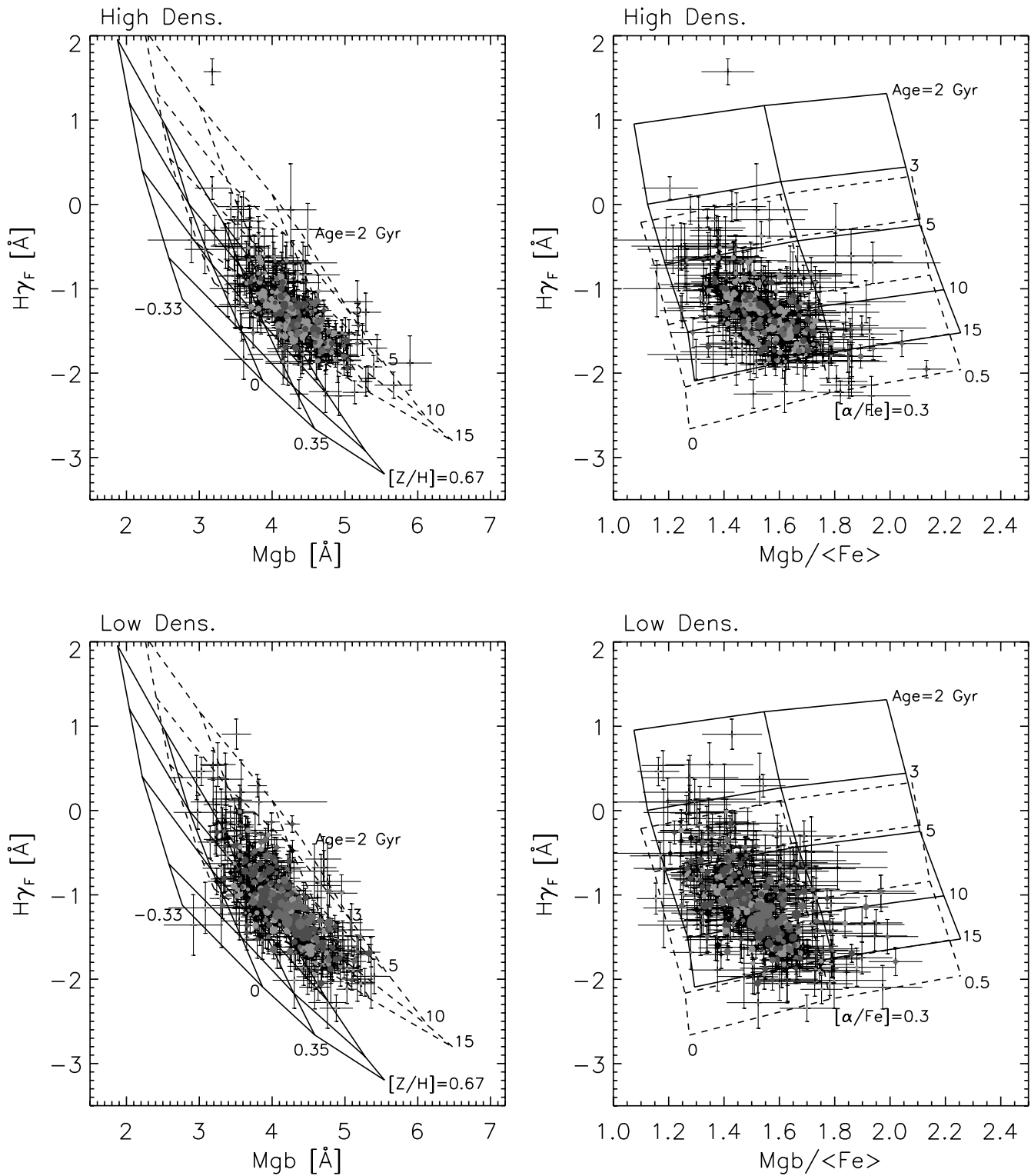


FIG. 15.—Same as Fig. 12, but with $H\gamma_F$ instead of $H\beta$. The left panels show clearly that these objects have nonsolar α -element abundance ratios (but see Appendix B for a discussion of whether flux calibration problems compromise the measurements in the lowest redshift bin). [See the electronic edition of the Journal for a color version of this figure.]

are very different, especially in dense regions. On the other hand, our derived correlations in the high-density regions are in slightly better agreement with those of the NOAO Fundamental Plane survey (Nelan et al. 2005) of clusters (*dashed curves*).

In the lower density regions, one might worry that our decision to compare low- and high-density environments by keep-

ing the slope of the correlations with σ fixed and simply fitting for an offset appears to be unreasonable for the $[Z/H]$ - σ relation. The slope of this relation appears to be steeper in the low-density regions. Allowing for this would bring it into better agreement with that of Thomas et al. (2005). But the significant differences at high densities remain.

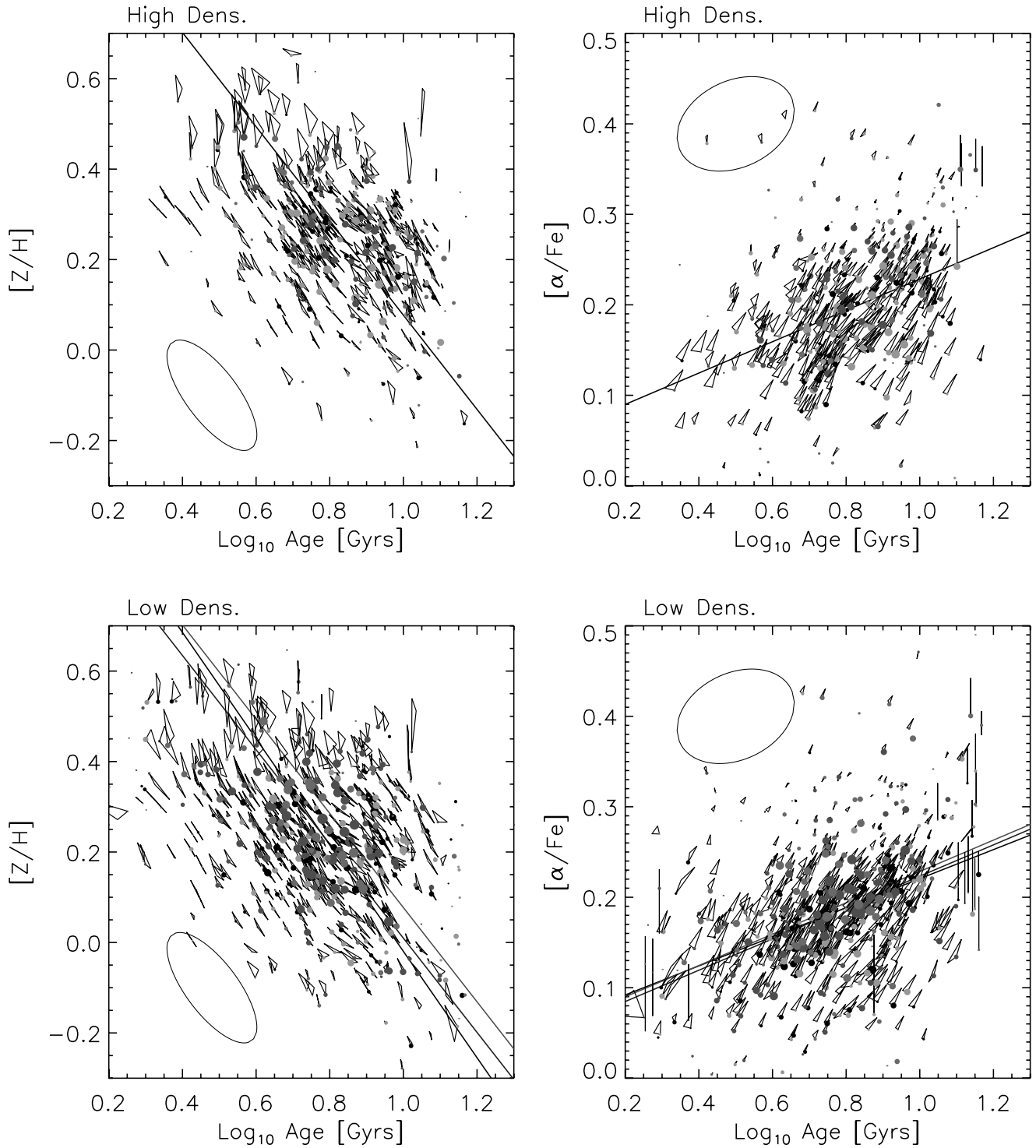


FIG. 16.—Same as Fig. 13, but with $H\gamma_F$ instead of $H\beta$. Here the anticorrelation between $[Z/H]$ and age is slightly steeper than before, and the correlation between $[\alpha/Fe]$ and age is steeper and tighter than before. (See Appendix B for a discussion of whether flux calibration problems compromise the results in the lowest redshift bin.) [See the electronic edition of the *Journal* for a color version of this figure.]

As a check, we have run our algorithm on the data analyzed by Thomas et al. (2005) and verified that the derived ages, metallicities, and α -enhancements we derive are within a few percent of those they obtained using a slightly different algorithm. For example, for an object with $(H\beta, Mg\ b, \langle Fe \rangle) = (1.59\ \text{\AA}, 4.73\ \text{\AA}, 2.84\ \text{\AA})$, our procedure returns an age of 10.7 Gyr, $[Z/H] = 0.26$, and $[\alpha/Fe] = 0.24$. Thus, differences in our methods used to derive ages, $[Z/H]$, and $[\alpha/Fe]$ from the model grids

are unimportant. Hence, we do not have a good explanation for why our correlations with σ , and the environmental dependences of these correlations, in our data set differ from the correlations in theirs; while our definitions of environment differ in detail, it is not obvious that this should lead to the relatively large qualitative differences we see.

Figures 15–17 show the result of repeating this analysis but using $H\gamma_F$ instead of $H\beta$. (This choice was motivated by

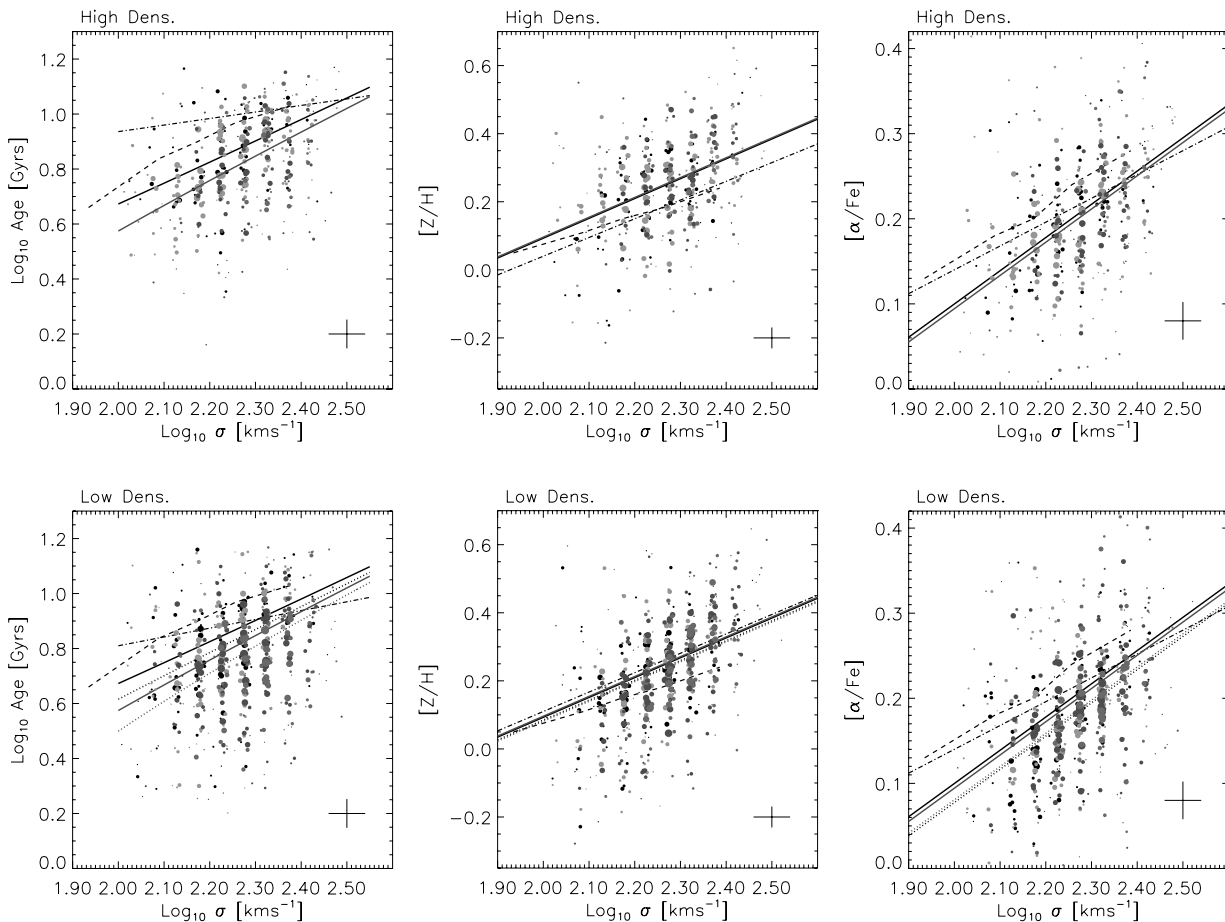


FIG. 17.—Same as Fig. 14, but with $H\gamma_F$ instead of $H\beta$. These panels show that the objects in the high-redshift population (*light lines*) are younger than their counterparts of the same σ at lower redshift (*black lines*). But there is no such trend for $[Z/H]$ or $[\alpha/Fe]$ (but see Appendix B for a discussion of whether flux calibration problems compromise the results in the lowest redshift bin). In addition, objects in lower density regions are slightly younger and less α -enhanced than their counterparts in denser regions. [See the electronic edition of the *Journal* for a color version of this figure.]

discussion in TMK04; we find similar results if we use $H\delta_A + H\gamma_A$ instead.) In general, this choice results in ages that are younger by 1 Gyr, but similar $[Z/H]$ and $[\alpha/Fe]$. This is true even if one allows for the possibility that there may be flux calibration problems for these Balmer lines at low redshifts (see Appendix B). (If there is a problem, then the ages we derive for the lowest redshift bin are overestimates, and the $H\gamma_F$ ages will be even smaller than those from $H\beta$. In addition, the metallicities will increase slightly. Applying these corrections would make the relative differences between the low- and high-redshift samples, at least in dense regions, more similar to the differences seen when $H\beta$ was used. But the overall offsets between the ages and metallicities estimated from these two sets of plots remains. Note that this difference from the $H\beta$ results is what one might have guessed from the differences shown in Fig. 11.) In particular, these differences are larger than any difference between the two environments.

7. DISCUSSION AND CONCLUSIONS

The properties of early-type galaxies show weak but significant correlations with environment. The Fundamental Plane indicates that cluster galaxies are ~ 0.08 mag arcsec $^{-2}$ fainter than their counterparts in low-density environments, and the scatter around the plane shows no significant dependence on environment (Fig. 3, Table 5). This is consistent with the hypothesis that cluster galaxies are only slightly older than their counterparts in the low-density environments or that metallicity ef-

fects on the Fundamental-Plane parameters counteract those of age.

Various indicators of chemical abundances also correlate weakly with environment: galaxies in low-density environments are slightly bluer, have experienced star formation more recently, and have weaker D4000 and Mg (Figs. 5–7), but these trends tend to be smaller than about 30% of the rms spread across the entire sample: i.e., the full distribution of observed values is not substantially broadened by environmental effects.

Galaxy color, and many absorption-line indices, correlate primarily with velocity dispersion. However, differences between cluster and low-density environment populations are seen even when the velocity dispersion is the same in both environments; the environment plays an important role in determining galaxy properties.

We discussed two methods of quantifying correlations with environment: both indicate that objects in clusters tend to be slightly older than those in less dense regions but that metallicity differences are small. The first method (§ 5) uses an argument that is relatively model independent and proceeds as follows: The absorption-line strengths evolve with redshift. Compared to their values at $z \sim 0$, Balmer lines were stronger, D4000 was weaker, Mg was weaker, and $\langle Fe \rangle$ was not very different at $z \sim 0.2$. If the high-redshift population is simply a passively evolved version of that locally (previous analysis suggests that this is a good approximation), then the observed evolution with

redshift can be used as a clock. In particular, comparison of the difference between cluster and low-density environment populations with the dependence on redshift (Figs. 8–10, Table 6) allows one to constrain the different relative roles of age and metallicity/ α -abundance on the various observed properties of galaxies.

For instance, our analysis shows, in a model-independent way, that Fe is less sensitive to age than is Mg. In addition, residuals from the Mg-luminosity relation show trends with evolution and environment similar to that for residuals from the color-magnitude relation. If we add the constraint that residuals from the color-magnitude relation are age indicators, then our data indicate that the rms spread in ages across the sample is slightly greater than ~ 1.5 Gyr, and the rms spread in $\log(\text{metallicity})$ is 0.08. In addition, galaxies in cluster environments are ~ 1 Gyr older than their counterparts in less dense environments, and the metallicity difference between the two environments is a negligible fraction of the full range of metallicities in the sample.

The second method (§ 6) uses single-burst stellar population synthesis models to interpret our data. These indicate that the objects at the lower redshifts in our sample are indeed consistent with being passively evolved versions of the objects at higher redshifts: we see evolution in age but not in metallicity $[Z/H]$ or the α -element abundance ratio $[\alpha/Fe]$. We find that age, $[Z/H]$, and $[\alpha/Fe]$ all increase with increasing velocity dispersion σ , in qualitative agreement with previous work. In addition, objects in dense regions tend to be older by less than 1 Gyr and have larger $[\alpha/Fe]$ (~ 0.02) than their counterparts of the same σ in less dense regions, but there is no evidence that objects in low-density regions are more metal-rich (Figs. 14 and 17). This suggests that in dense regions, the stars in early-type galaxies formed at slightly earlier times, and on a slightly shorter timescale, than in less dense regions. This is in qualitative agreement with a number of recent results (e.g., Thomas et al. 2005; Carretero et al. 2004). Whereas these qualitative conclusions do not depend on which absorption lines are used to interpret the data, quantitative conclusions do: use of $H\beta$ leads to systematically older ages than does $H\gamma_F$.

We began with the statement that the monolithic and stochastic models make different predictions for how early-type galaxy properties should depend on environment. While the analyses presented here do not answer the question of which model is correct, we feel that they provide a useful method for addressing this issue. In particular, it will be interesting to see whether these models are able to reproduce the weak environmental dependence of formation time and timescale suggested by our data.

Funding for the creation and distribution of the SDSS Archive has been provided by the Alfred P. Sloan Foundation, the Participating Institutions, the National Aeronautics and Space Administration, the National Science Foundation, the US Department of Energy, the Japanese Monbukagakusho, and the Max Planck Society. The SDSS Web site is at <http://www.sdss.org>.

The SDSS is managed by the Astrophysical Research Consortium for the Participating Institutions. The Participating Institutions are the University of Chicago, Fermilab, the Institute for Advanced Study, the Japan Participation Group, The Johns Hopkins University, the Korean Scientist Group, Los Alamos National Laboratory, the Max Planck Institute for Astronomy, the Max Planck Institute for Astrophysics, New Mexico State University, the University of Pittsburgh, Princeton University,

the United States Naval Observatory, and the University of Washington.

APPENDIX A

EVOLUTION AND SELECTION EFFECTS

In the main text we present estimates of how index strengths in the population have evolved. In all cases, these estimates were made by computing residuals from the index- σ relation rather than from the index-magnitude relation. This was done for two reasons. First, for almost all indices, the index- σ relation is considerably tighter than the index-luminosity relation, so a small amount of evolution is more easily detected. Second, the velocity dispersion is expected to evolve much less than the luminosity, so it is a more direct surrogate for estimating evolution at fixed mass.

However, the SDSS sample is magnitude-limited. Therefore, care must be taken to account for the effects of this selection before interpreting trends with redshift as being due to evolution. To illustrate, Figure 18 shows the Mg-luminosity, Mg- σ , Fe-luminosity, and Fe- σ correlations measured using objects in different redshift bins (bins are adjacent with edges at $z = 0.05, 0.07, 0.09, 0.12, 0.14$, and 0.17 , as in the main text). The plot uses luminosities corrected for evolution to $z = 0$. In all cases, the circles show the median values of the index (Mg or Fe) in small bins in luminosity or σ . Hatched regions show the range that includes 68% of the objects. (Mg and Fe are representative of most of the other indices presented in the main text.)

At any given redshift, Mg correlates with both luminosity and σ , whereas Fe correlates with σ but not with luminosity. The Mg- σ correlation is significantly tighter than Mg-luminosity. Both Mg- σ and Fe- σ appear to evolve. In the case of Fe- σ , the apparent evolution is differential. One might have thought that because Fe does not correlate with luminosity, measurement of the Fe- σ relation can be made without worrying about the magnitude limit of the sample, so the differential evolution is real. The following model shows that this is not the case.

Let I_* , M_* , and V_* and σ_{II} , σ_{MM} , and σ_{VV} denote the mean and rms values of index strength, absolute magnitude, and $\log(\text{velocity dispersion})$ in the entire population at a given redshift (i.e., not just the part that was selected for observation). Let $\mathcal{I} = (I - I_*)/\sigma_{II}$, $\mathcal{M} = (M - M_*)/\sigma_{MM}$, and $\mathcal{V} = (V - V_*)/\sigma_{VV}$, and define $\xi_{IM} \equiv \langle \mathcal{I}\mathcal{M} \rangle$, $\xi_{IV} \equiv \langle \mathcal{I}\mathcal{V} \rangle$, and $\xi_{VM} \equiv \langle \mathcal{V}\mathcal{M} \rangle$, where the angle brackets denote averages over the entire population. The mean value of I at fixed M is

$$\langle \mathcal{I} | \mathcal{M} \rangle = \mathcal{M} \xi_{IM}, \quad (\text{A1})$$

and similar expressions hold for the other pairs of observables: e.g., $\langle \mathcal{I} | \mathcal{V} \rangle = \mathcal{V} \xi_{IV}$, $\langle \mathcal{V} | \mathcal{M} \rangle = \mathcal{M} \xi_{VM}$, and $\langle \mathcal{M} | \mathcal{I} \rangle = \mathcal{I} \xi_{IM}$. Similarly, the mean I at fixed V and M is

$$\langle \mathcal{I} | \mathcal{M}, \mathcal{V} \rangle = \mathcal{M} \frac{\xi_{IM} - \xi_{IV}\xi_{MV}}{1 - \xi_{MV}^2} + \mathcal{V} \frac{\xi_{IV} - \xi_{IM}\xi_{MV}}{1 - \xi_{MV}^2}, \quad (\text{A2})$$

with obvious permutations giving $\langle \mathcal{M} | \mathcal{V}, \mathcal{I} \rangle$ and $\langle \mathcal{V} | \mathcal{I}, \mathcal{M} \rangle$.

If the correlation between index and magnitude is entirely due to the index- σ and magnitude- σ correlations, then $\xi_{IM} = \xi_{IV}\xi_{VM}$. (Bernardi et al. [2005] show that this is true for the color- σ relation.) In this case, $\langle \mathcal{I} | \mathcal{M}, \mathcal{V} \rangle = \mathcal{V} \xi_{IV}$ is independent of \mathcal{M} , so the index- σ relation can be measured directly from the observed data without worrying about the magnitude

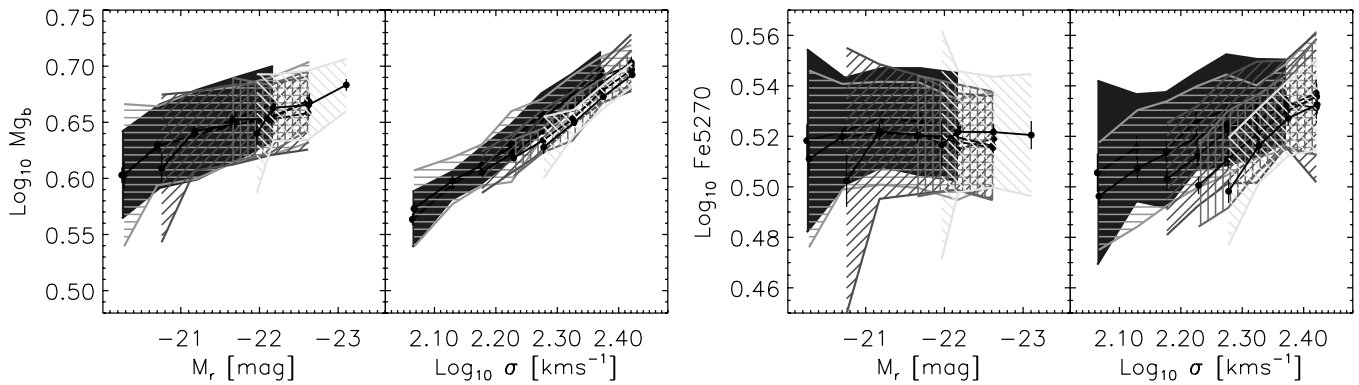


FIG. 18.—*Left panels:* Correlation between Mg *b* and magnitude (*left*) and velocity dispersion (*right*). Hatched regions show different redshift bins. *Right panels:* Correlation between Fe5270 and magnitude (*left*) and velocity dispersion (*right*). The differential evolution seen in the Fe- σ relation is due to selection effects (see text for details). [See the electronic edition of the Journal for a color version of this figure.]

limit (e.g., Bernardi et al. 2005). Note that this is despite the fact that there is an index-magnitude relation.

Now consider what happens if the index does not correlate with magnitude (as is the case for Fe): $\xi_{IM} = 0$. In this case, $\langle \mathcal{I} | \mathcal{M}, \mathcal{V} \rangle = (\mathcal{V} - \xi_{MV} \mathcal{M}) \xi_{IV} / (1 - \xi_{MV}^2)$. Because this expression depends on absolute magnitude, measuring the mean index strength as a function of velocity dispersion using galaxies observed in a fixed redshift bin of a magnitude-limited sample will lead to a biased estimate of the true correlation.

To illustrate this bias, a mock galaxy catalog was generated by distributing objects uniformly in a comoving volume with $p(M, V, I)$ a multivariate Gaussian. The parameters of this Gaussian were chosen to match the distribution of luminosities and velocity dispersions in the catalog (from Bernardi et al. 2003b): $\sigma_{MM} = 0.84$, $\sigma_{VV} = 0.11$, $\xi_{MV} = -0.77$, $\sigma_{II} = 0.05$, and $\xi_{IV} = 0.25$. (The values of σ_{II} and ξ_{IV} were chosen to match the Fe- σ relation.)

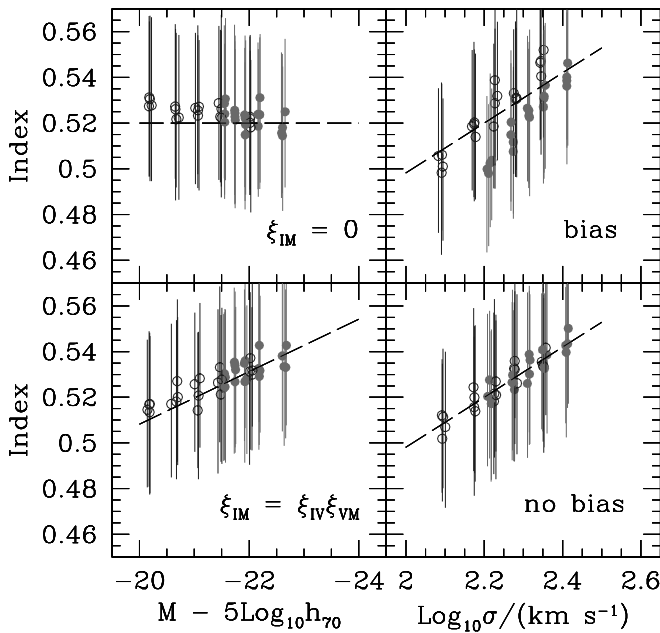


FIG. 19.—Index-luminosity and index- σ relations measured from a magnitude-limited catalog in low- z (*open circles*) and high- z bins (*filled circles*). Error bars show the values at 25% and 75%. Dashed lines show the true relations. The top panel shows a model in which index strength does not correlate with magnitude, and the bottom panel shows a model in which the index-magnitude correlation is entirely due to the index- σ and magnitude- σ correlations. Note the bias in the top right panel, which appears to indicate differential evolution. [See the electronic edition of the Journal for a color version of this figure.]

Figure 19 (*top panels*) shows the index-magnitude and index- σ relations if $\xi_{IM} = 0$. Dashed lines show the input relations, and symbols show the relations measured using objects that have apparent magnitudes between 14.5 and 17.45 but have redshifts between 0.05 and 0.07 (*open circles*) or 0.12 and 0.14 (*filled circles*). Different sets of symbols at each bin are for different realizations of mock catalogs that have approximately the same number of objects in each redshift bin as the data (~ 1500 for the redshift bins shown). The apparent steepening of the index- σ relation with redshift is *entirely* due to the magnitude limit. This demonstrates that direct measurement of the index- σ relation using objects in an apparent magnitude-limited catalog can lead to a biased estimate of the true relation, even if the index itself does not correlate with absolute magnitude.

The bottom panel is similar, except that it has $\xi_{IM} = \xi_{IV} \xi_{VM}$. In this case, the index-luminosity and index- σ relations measured in the magnitude-limited sample are unbiased estimates of the true relation, even though index strength correlates with magnitude, in agreement with the model described above.

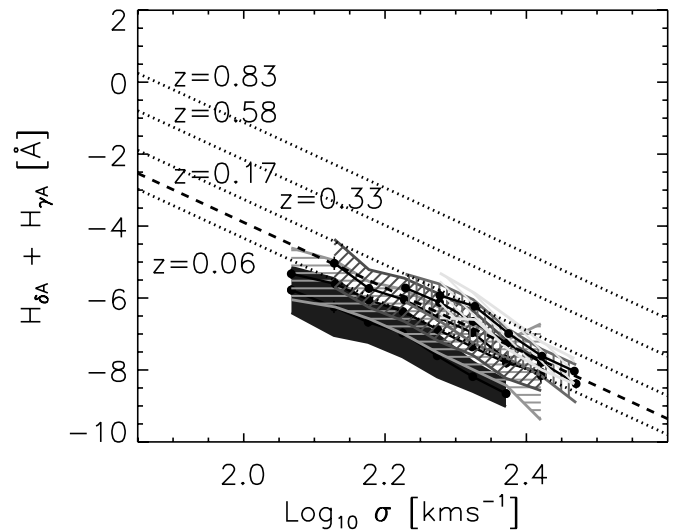


FIG. 20.—Comparison of the correlation between $H\delta_A + H\gamma_A$ and velocity dispersion in our sample (shaded regions show different redshift bins) with the relation measured using galaxies in clusters at redshifts $z = 0.06, 0.33, 0.58$, and 0.83 (*dotted lines*; Kelson et al. 2001). The dashed line shows the relation obtained by interpolating between the 0.06 and 0.33 lines to $z = 0.17$ for ease of comparison with our data. While the SDSS data have the same slope, they have a smaller zero point at low redshift. Thus, the apparent evolution in the SDSS sample is about a factor of 3 larger than indicated by the dotted lines. [See the electronic edition of the Journal for a color version of this figure.]

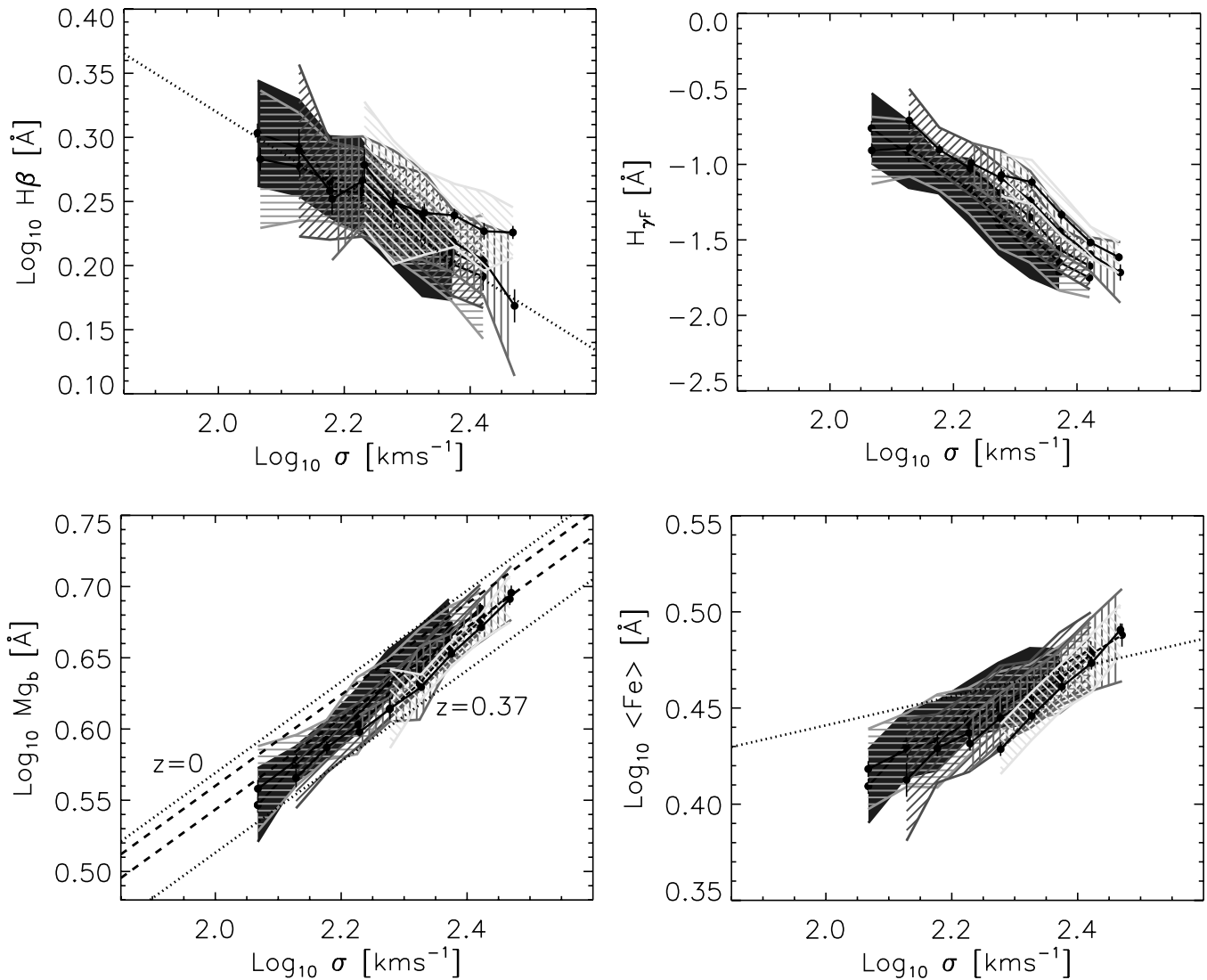


FIG. 21.—Correlation between the line-index strengths (smoothed to Lick resolution) used in § 6 and velocity dispersion. The top left and right panels show the anticorrelation between $H\beta$ and $H\gamma_F$ with σ . The bottom left and right panels show that $Mg\ b$ and $\langle Fe \rangle$ are positively correlated with σ . Hatched colored regions show these relations in different redshift bins. Dotted lines for $H\beta$ and $\langle Fe \rangle$ show the correlations from Jørgensen (1997). For the $Mg\ b$ - σ relation, dotted lines show the relation at $z = 0$ and 0.37 reported by Bender et al. (1996). Dashed lines show their results interpolated to $z = 0.06$ and 0.17 to simplify comparison with our results. The apparent rapid differential evolution of the Fe - σ relation is a selection effect. [See the electronic edition of the *Journal* for a color version of this figure.]

Thus, for the Fe - σ relation in Figure 18, most of the difference between the low- and high-redshift bins is a selection effect. The Mg -luminosity correlation is slightly weaker than $\xi_{IV\xi_{VM}}$, so it too is biased by selection effects, although by a smaller amount. In all cases, the selection effect is more dramatic at low σ . Since we are interested in estimating how these indices evolve, we estimate evolution from the highest bin in σ for which we have at least 1000 objects over $0.06 \leq z \leq 0.17$: i.e., $2.35 \leq \sigma \leq 2.4$. Since even this may be slightly affected by selection effects, it gives an upper limit to the true evolution.

APPENDIX B

SDSS FLUX CALIBRATION AND BALMER LINE STRENGTHS

The main text notes that flux calibration problems around $4000\ \text{\AA}$ may affect measurements of Balmer line strengths and D4000. Evidence that this is a serious concern is presented in Figure 20. Dotted lines show the correlation between $H\delta_A + H\gamma_A$

and velocity dispersion measured by Kelson et al. (2001) using early-type galaxies in four clusters at the redshifts indicated. They find that the zero point of the relation evolves but are not able to conclude whether the slope does or not.

The shaded regions show the correlation between $H\delta_A + H\gamma_A$ and velocity dispersion in our sample in the same redshift bins used in the main text ($0.05 < z < 0.07$, $0.07 < z < 0.09$, $0.09 < z < 0.12$, $0.12 < z < 0.14$, and $0.14 < z < 0.20$). Note that our SDSS data produce the same slope as the data from the literature, but the zero points are quite different at low redshift.

What is most relevant to the analysis in the main text is the rate at which the line strengths evolve. Since flux calibration problems affect observed wavelengths, they appear as redshift-dependent effects when studying features at fixed rest-frame wavelength. Figure 20 demonstrates that the apparent evolution in the SDSS sample is about 3 times larger than that seen by Kelson et al. (2001). Since we already have reason to believe that flux calibration is difficult around $\lambda_{\text{obs}} = 4000\ \text{\AA}$, so it is possible that the low-redshift bins are more strongly affected than

the bins at higher redshift, this strongly suggests that flux calibration systematics are affecting the SDSS measurement. Therefore, in the main text we show the apparent evolution using the raw measurements, as well as the result of dividing the apparent evolution by a factor of 3.

Figure 21 shows our measurements of the correlations between $H\beta$, $H\gamma_F$, $Mg\ b$, and $\langle Fe \rangle$ with velocity dispersion. These are the indices we use in our study of single-burst stellar population synthesis models (§ 6). Our measurements are in reasonable agreement with previous work, with the exception of $Mg\ b$. Our $Mg\ b$ values are offset to smaller values than those of Bender et al. (1996); this offset is not due to the fact that Bender et al. aperture correct both $Mg\ b$ and σ to a fixed physical scale, whereas we correct to $r_e/8$. Shifting our values upward so they agree with the literature makes little qualitative difference to our conclusions about the ages, metallicities, and α -enhancements in our sample.

As another check, Figure 22 shows that the Mg_2 - σ correlation and its evolution are consistent with previous work (Bernardi et al. 1998). Using Mg_2 in place of $Mg\ b$, and making the corresponding change in the SSP models, makes no difference to our findings.

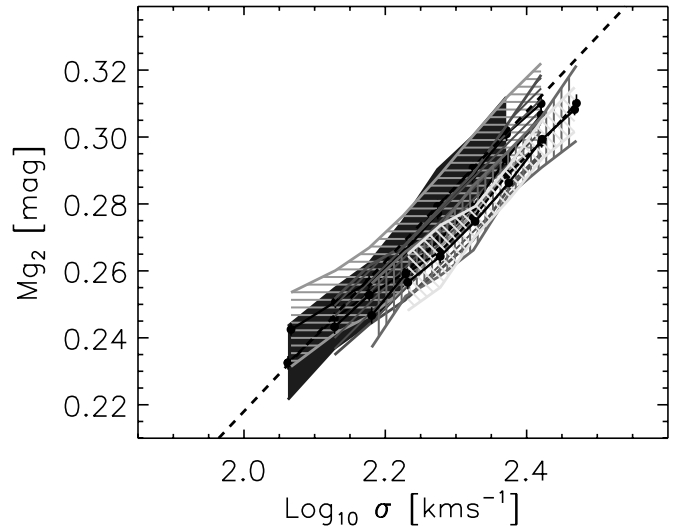


FIG. 22.—Comparison of correlation between Mg_2 and σ reported by Bernardi et al. (1998; dashed line) and the relation in the present data set (hatched colored regions show the relation in different redshift bins). [See the electronic edition of the Journal for a color version of this figure.]

REFERENCES

- Abazajian, K., et al. 2003, *AJ*, 126, 2081
 Balogh, M. L., Christlein, D., Zabludoff, A. I., & Zaritsky, D. 2001, *ApJ*, 557, 117
 Balogh, M. L., Morris, S. L., Yee, H. K. C., Carlberg, R. G., & Ellingson, E. 1999, *ApJ*, 527, 54
 Balogh, M., et al. 2004, *MNRAS*, 348, 1355
 Bekki, K., Couch, W. J., & Shioya, Y. 2001, *PASJ*, 53, 395
 Bender, R., Ziegler, B., & Bruzual, G. 1996, *ApJ*, 463, L51
 Bernardi, M., Renzini, A., da Costa, L. N., Wegner, G., Alonso, M. V., Pellegrini, P. S., Rit , C., & Willmer, C. N. A. 1998, *ApJ*, 508, L143
 Bernardi, M., Sheth, R. K., Nichol, R. C., Schneider, D. P., & Brinkmann, J. 2005, *AJ*, 129, 61
 Bernardi, M., et al. 2003a, *AJ*, 125, 1817
 ———. 2003b, *AJ*, 125, 1849
 ———. 2003c, *AJ*, 125, 1866
 ———. 2003d, *AJ*, 125, 1882
 Blakeslee, J. P., et al. 2003, *ApJ*, 596, L143
 Blanton, M. R., Lupton, R. H., Maley, F. M., Young, N., Zehavi, I., & Loveday, J. 2003, *AJ*, 125, 2276
 Bower, R. G., Lucey, J. R., & Ellis, R. S. 1992a, *MNRAS*, 254, 589
 ———. 1992b, *MNRAS*, 254, 601
 Bruzual, G., & Charlot, S. 2003, *MNRAS*, 344, 1000
 Carretero, C., Vazdekis, A., Beckman, J. E., Sanchez-Blazquez, P., & Gorgas, J. 2004, *ApJ*, 609, L45
 Colless, M., Burstein, D., Davies, R. L., McMahan, R. K., Saglia, R. P., & Wegner, G. 1999, *MNRAS*, 303, 813
 Djorgovski, S., & Davis, M. 1987, *ApJ*, 313, 59
 Dressler, A. 1980, *ApJ*, 236, 351
 Dressler, A., Lynden-Bell, D., Burstein, D., Davies, R. L., Faber, S. M., Terlevich, R. J., & Wegner, G. 1987, *ApJ*, 313, 42
 Eisenstein, D. J. 2003, *ApJ*, 586, 718
 Eisenstein, D. J., et al. 2001, *AJ*, 122, 2267
 Faber, S. M., & Jackson, R. 1976, *ApJ*, 204, 668
 Fukugita, M., Ichikawa, T., Gunn, J. E., Doi, M., Shimasaku, K., & Schneider, D. P. 1996, *AJ*, 111, 1748
 Gunn, J. E., & Gott, J. R., III. 1972, *ApJ*, 176, 1
 Gunn, J. E., et al. 1998, *AJ*, 116, 3040
 Hogg, D. W., Schlegel, D. J., Finkbeiner, D. P., & Gunn, J. E. 2001, *AJ*, 122, 2129
 Hogg, D. W., et al. 2004, *ApJ*, 601, L29
 J rgensen, I. 1997, *MNRAS*, 288, 161
 Kauffmann, G. 1996, *MNRAS*, 281, 487
 Kauffmann, G., & Charlot, S. 1998, *MNRAS*, 294, 705
 Kauffmann, G., et al. 2003, *MNRAS*, 346, 1055
 Kelson, D. D., Illingworth, G. D., Franx, M., & van Dokkum, P. G. 2001, *ApJ*, 552, L17
 Kodama, T., Arimoto, N., Barger, A. J., & Arag n-Salamanca, A. 1998, *A&A*, 334, 99
 Kuntschner, H. 2004, *A&A*, 426, 737
 Kuntschner, H., Lucey, J. R., Smith, R. J., Hudson, M. J., & Davies, R. L. 2001, *MNRAS*, 323, 615
 Lacey, C., & Cole, S. 1993, *MNRAS*, 262, 627
 Lupton, R., Gunn, J. E., Ivezi , Z., Knapp, G. R., Kent, S., & Yasuda, N. 2001, in *ASP Conf. Ser. 238, Astronomical Data Analysis Software and Systems X*, ed. F. R. Harnden, Jr., F. A. Primini, & H. E. Payne (San Francisco: ASP), 269
 Miller, C. J., et al. 2005, *AJ*, 130, 968
 Mo, H. J., & White, S. D. M. 1996, *MNRAS*, 282, 347
 Moore, B., Lake, G., Quinn, T., & Stadel, J. 1999, *MNRAS*, 304, 465
 Nelan, J. E., Smith, R. J., Hudson, M. J., Wegner, G. A., Lucey, J. R., Moore, S. A. W., Quinney, S. J., & Suntzeff, N. B. 2005, *ApJ*, 632, 137
 Petrosian, V. 1976, *ApJ*, 209, L1
 Pier, J. R., Munn, J. A., Hindsley, R. B., Hennessy, G. S., Kent, S. M., Lupton, R. H., & Ivezi , Z. 2003, *AJ*, 125, 1559
 Poveda, A. 1961, *ApJ*, 134, 910
 Sandage, A., & Visvanathan, N. 1978a, *ApJ*, 223, 707
 ———. 1978b, *ApJ*, 225, 742
 Smith, J. A., et al. 2002, *AJ*, 123, 2121
 Stoughton, C., et al. 2002, *AJ*, 123, 485
 Strauss, M. A., et al. 2002, *AJ*, 124, 1810
 Tantal , R., & Chiosi, C. 2004, *MNRAS*, 353, 917
 Thomas, D., Maraston, C., & Bender, R. 2003, *MNRAS*, 339, 897 (TMB03)
 Thomas, D., Maraston, C., Bender, R., & de Oliveira, C. M. 2005, *ApJ*, 621, 673
 Thomas, D., Maraston, C., & Korn, A. 2004, *MNRAS*, 351, L19 (TMK04)
 Trager, S. C., Faber, S. M., Worthey, G., & Gonz lez, J. J. 2000, *AJ*, 119, 1645
 Trager, S. C., Worthey, G., Faber, S. M., Burstein, D., & Gonz lez, J. J. 1998, *ApJS*, 116, 1
 Tripicco, M. J., & Bell, R. A. 1995, *AJ*, 110, 3035
 Wake, D. A., Collins, C. A., Nichol, R. C., Jones, L. R., & Burke, D. J. 2005, *ApJ*, 627, 186
 White, S. D. M., & Frenk, C. 1991, *ApJ*, 379, 52
 White, S. D. M., & Rees, M. J. 1978, *MNRAS*, 183, 341
 Worthey, G., Faber, S. M., Gonzalez, J. J., & Burstein, D. 1994, *ApJS*, 94, 687
 Worthey, G., & Ottaviani, D. L. 1997, *ApJS*, 111, 377
 York, D. G., et al. 2000, *AJ*, 120, 1579